

1
2
3
4 **High pressure behavior and structural transition of beryl-type johnkoivulaite,**
5 **Cs(Be₂B)Mg₂Si₆O₁₈**

6
7 **G. Diego Gatta^{1*}, Martin Ende², Sofija Miloš², Nicola Rotiroti¹,**

8 **Aaron C. Palke³, Ronald Miletich²**

9 ¹Università degli Studi di Milano, Dipartimento di Scienze della Terra, Via Botticelli 23, I-20133 Milano, Italy

10 ²University of Vienna, Department of Mineralogy and Crystallography, A-1090 Wien, Austria

11 ³Gemological Institute of America, Carlsbad, CA 92008, USA
12
13

14 **Abstract**

15 The beryl-group mineral johnkoivulaite, Cs(Be₂B)Mg₂Si₆O₁₈, was compressed hydrostatically in a
16 diamond-anvil cell up to 10.2 GPa. *In-situ* Raman spectroscopy and X-ray crystallography revealed
17 a *P6/mcc*-to-*P $\bar{3}$ c1* (second-order) phase transition on isothermal compression at the critical transition
18 pressure $P_c = 4.13 \pm 0.07$ GPa. The elastic parameters determined for the volume elasticity of the two
19 polymorphs correspond to a Birch-Murnaghan equation of state with $K_0 = 148 \pm 2$ GPa and $K' = 0$ for
20 $P < P_c$ and $K_0 = 75.5 \pm 0.9$ GPa with $K' = 4$ for $P > P_c$. The low-*P* polymorph shows anomalously
21 linear compression behavior, as reported for several other beryl-derived framework structures. The
22 high-*P* polymorph, which was found to follow a $a' = a \cdot \sqrt{3}$, $c' = c$ superstructure according to *P $\bar{3}$ c1*,
23 is almost twice as compressible as its low-*P* form. This is unique for any beryl-derived structure and
24 can be attributed to the high degree of freedom for atomic displacements in the superstructure. The
25 reduced symmetry can also be understood as the effect of the driving mechanism of the
26 transformation. The extra-framework Cs channel components counteract any lateral deformation of
27 the channels parallel to [0001] within the microporous framework and, similar to pezzottaite, are
28 responsible for maintaining the trigonal/hexagonal lattice metrics.
29

30 **Keywords:** beryl-type structure, johnkoivulaite, high pressure, structural transition, second-order
31 phase transition, superstructure
32
33

34

35

36 Introduction

37 The beryl-type structure is an outstanding structure representing a non-holotetrahedral
38 framework, with a pronounced one-dimensional porosity in the form of channels running along
39 [0001]. It is represented in nature by several beryllium silicate minerals, such as beryl $\text{Be}_3\text{Al}_2(\text{Si}_6\text{O}_{18})$,
40 stoppaniite $\text{Be}_3\text{Fe}_2(\text{Si}_6\text{O}_{18})$, and bazzite, $\text{Be}_3\text{Sc}_2(\text{Si}_6\text{O}_{18})$, whose crystal structures consist of the
41 symmetry-determining $[\text{Si}_6\text{O}_{18}]^{6-}$ silicate ring units that predetermine the hexagonal archetype
42 microporous framework (*e.g.*, Bragg and West 1926; Gibbs et al. 1968; Artioli et al. 1993; Armbruster
43 et al. 1995; Ferraris et al. 1998; Della Ventura et al. 2000). Any deviation from the beryl-aristotype
44 $P6/mcc$ symmetry originates from stoichiometric substitution, such as in cordierite $\text{Al}_3\text{Mg}_2(\text{AlSi}_5\text{O}_{18})$
45 and sekaninaite $\text{Al}_3\text{Fe}_2(\text{AlSi}_5\text{O}_{18})$, where the substitution of 1/3 of the silicon atoms on the $T2$ site
46 within the ring units, and the simultaneous occupation of Si on the $T1$ site, leads to symmetry-
47 breaking orthorhombic $Cmcm$ cation distribution (Armbruster 1985; Redfern et al. 1989; Daniels et
48 al. 1994; Malcherek et al. 2001). While the cation redistribution on the tetrahedral $T1$, $T2$ and the
49 octahedral M sites does not affect the total charge balance of the framework, both in pezzottaite,
50 $\text{Cs}(\text{Be}_2\text{Li})\text{Al}_2\text{Si}_6\text{O}_{18}$, and johnkoivulaite, $\text{Cs}(\text{Be}_2\text{B})\text{Mg}_2\text{Si}_6\text{O}_{18}$, the stoichiometric substitution of one
51 third of the Be by either lithium or boron at the $T1$ position leads to a formal charge deficiency within
52 the framework (Yakubovich et al. 2009; Gatta et al. 2012; Lambruschi et al. 2014; Palke et al. 2021).
53 This, in turn, requires charge balance through additional extra-framework cations located within the
54 one-dimensionally infinite channel mentioned above. The structures of pezzottaite and johnkoivulaite
55 are characterized by the intercalation of a significant fraction of alkali cations, preferably high Cs
56 contents, within the cavities of the existing one-dimensional channels. At least for pezzottaite, a
57 resultant lower symmetry and the formation of a trigonal superstructure, according to the $R\bar{3}c$ space
58 group, could be demonstrated for the existing Li-Be cation ordering.

59 The ability to incorporate Cs in the microporous framework makes beryl-type compounds of
60 interest in the materials science community. In particular, immobilization of Cs-137 makes the
61 physicochemical properties of this potential host structure important for possible technological
62 applications. Thermodynamic properties and phase stabilities are an important focus of research. The
63 two most prominent representatives of this mineral group, *i.e.*, cordierite and beryl, moreover are
64 characterized by their petrological importance. Cordierite is a stable phase in contact metamorphic
65 pelitic rocks or in high-grade regionally metamorphosed schists, gneisses, and granulites. Beryl is a
66 host of Be, a rare lithophile element, in highly evolved S-type granites, granitic pegmatites,
67 hydrothermal deposits related to granite (*e.g.*, greisen), volcanogenic hosted beryllium deposits, or
68 metamorphic rocks (*i.e.*, emerald-bearing schists) (Hess 1969; Deer et al. 1992; Spear 1993; Barton
69 and Young 2002; García-Moreno et al. 2007; Klein and Philpotts 2012). Potential phase

70 transformations, their mechanisms and the knowledge of the factors stabilizing or destabilizing the
71 structure are the subject of numerous investigations under variable pressure and temperature
72 conditions. Among others, the isothermal equations of state as well as thermal expansion coefficients
73 for beryl, cordierite and also pezzottaite have been investigated in the past. In addition to the long-
74 known order-disorder transformations, such as that of cordierite-iolite, transitions under pressure into
75 new, denser polymorphic forms have been reported, including transformation into the heavily
76 twinned triclinic form of cordierite (Miletich et al. 2014a; Finkelstein et al. 2015), the likely formation
77 of modulated beryll-II at pressures beyond 12 GPa (O'Bannon and Williams 2016), or the second-
78 order transition of pezzottaite at 4 GPa from $R\bar{3}c$ to $R3c$ (Ende et al. 2021). A remarkable common
79 feature of all high-pressure investigations is the extraordinary compression behavior with respect to
80 the pressure dependency of the bulk modulus, regardless of whether a transformation was observed
81 or not. In all cases, values for $\partial K/\partial P$ have been determined to be close to zero or even negative, and
82 thus suggest an anomalous elastic behavior for members of this structural family.

83 The most recently described new mineral species johnkoivulaite is, after pezzottaite, the
84 second and only other representative of the beryl-group with Cs-stuffed host-guest structure required
85 for the stoichiometric charge compensation of the framework. Incorporation of extra-framework
86 components, *e.g.* H₂O, CO₂, Ar or even small fractions of alkali cations, has been reported for some
87 of the mineral phases structurally related to beryl (*e.g.*, Armbruster 1985b,1986; Charoy et al. 1996;
88 Kolesov and Geiger 2000; Mashkovtsev and Thomas 2005). Investigations of static compression, and
89 its dependence on the type and concentration of molecules embedded within channels, also showed
90 a demonstrable influence on the lattice elastic properties (*e.g.*, Miletich et al. 2014a,b; Scheidl et al.
91 2014). Nevertheless, pezzottaite was investigated as the very first phase with considerable contents
92 of stoichiometrically required extra-framework alkali cations. Despite the analogy regarding the
93 stoichiometric formula, the different symmetry alone is striking, so that high-pressure studies on this
94 new mineral appeared necessary in the context of understanding the extraordinary behavior of this
95 structure type. In order to evaluate the lattice properties and structural changes, *in-situ* high-pressure
96 investigations were carried out on a single-crystal sample from the only so far known johnkoivulaite
97 specimen, as compressed hydrostatically by using diamond-anvil cell techniques.

98

99 **Materials and methods**

100 ***Sample material and high-pressure sample environment***

101 All investigations in this study were performed on a small fragment extracted from the original
102 type material from Mogok, Myanmar (type specimen deposited under no. 41653, in the collection of
103 the Gemological Institute of America Museum) as described in Palke et al. (2021). The chemical
104 composition can be assumed to correspond to the formula
105 $(\text{Cs}_{0.85}\text{K}_{0.10})(\text{Be}_{1.88}\text{B}_{1.12})(\text{Mg}_{1.66}\text{Fe}_{0.27}\text{Al}_{0.05})\text{Si}_{5.98}\text{O}_{18}$, as determined earlier by means of electron
106 microprobe analyses, laser ablation ICP-MS analyses and infrared spectroscopy. The investigations
107 were carried out on crystal fragments from a double-sided polished crystal plate (measuring 40 ± 2
108 μm in thickness), which was fabricated in arbitrary orientation from an unoriented crystal grain. High-
109 pressure sample environment was provided by using an ETH-type diamond anvil cell (Miletich et al.
110 2000), using anvils with 0.6 mm culets and compressing in either cryogenically loaded argon or a
111 conventional ethanol-methanol mixture as the hydrostatic pressure-transmitting medium. Details on
112 the individual loadings, sample dimensions, the gasket thicknesses and borehole diameters are
113 provided in Table S1 in the supplementary material. Pressures on isothermal compression were
114 calibrated using the established quartz and ruby pressure gauges (Angel et al. 1997; Jacobsen et al.
115 2008; Scheidl et al. 2016) to within estimated uncertainties of less than ± 0.01 GPa (for quartz) and
116 ± 0.06 GPa (for ruby). For single-crystal X-ray diffraction experiment at ambient atmospheric
117 pressure, the crystal fragment was mounted on a Mitigen Kapton loop.

118

119 ***Raman spectroscopy***

120 High-pressure Raman spectroscopic investigations were carried on crystals compressed in
121 argon up to 10.19 GPa by means of a confocal *Horiba Jobin Yvon LabRAM-HR 800* spectrometer
122 using a Nd:YAG laser source, with a wavelength of 532.05 nm. The spectrometer was equipped with
123 an *Olympus BX41* microscope, and its *Olympus LMPlanFL N 50 \times objective with a long working
124 distance of 10.6 mm was used for all measurements with the ETH-type DAC. A total of 64 high-
125 pressure spectra were recorded (a series of 19 spectra on compression and a subsequent series of 45
126 on decompression), covering a spectral range from 50 to 1250 cm^{-1} Raman shift, at 3×60 seconds
127 exposure time per step. For all measurements, a diffraction grating with 600 lines per mm was used.
128 Spectra were acquired using the *LabSpec 6* software (*HORIBA Scientific*) and *Peakfit v.4* (*Systat*
129 *Software Inc.*) software was used for background subtraction as well as for the determination of the
130 band position. All Raman spectra were fitted with the Gauss-Lorentz-area method.*

131

132 *Single-crystal X-ray diffraction*

133 The unit-cell parameters were determined from measurements on a Stoe AED II
134 diffractometer (Eulerian cradle, graphite-monochromatized Mo-radiation from 50 kV / 30 mA sealed-
135 tube source, point detector). Data acquisition and refinement were performed using the SINGLE
136 software (Angel and Finger 2011). In addition to the sample crystal, a quartz single crystal was added
137 inside the pressure chamber and its cell parameters were measured for precise pressure determination.
138 Applying the 8-position centering mode (King and Finger 1979), both unconstrained and symmetry-
139 constrained unit-cell parameters were determined for 16 pressure points in the range between 0.0001
140 and 8.41 GPa. Equation-of-state (EoS) parameters were fitted to the P - V data before and after the
141 supposed critical transition pressure, using the software EoSFit7GUI (Gonzalez-Platas et al. 2016).

142 X-ray intensity data were collected at 0.0001, 1.65 ± 0.05 and 6.50 ± 0.05 GPa, using a Stoe
143 StadiVari diffractometer system equipped with a Dectris Pilatus 300K detector with a $450\mu\text{m}$ silicon
144 layer and an air-cooled Incoatec I μ S molybdenum microfocus tube (operated at 50 kV / 1 mA, beam
145 diameter of $\sim 110\ \mu\text{m}$ FWHM). Details of the instrument settings for the XRD intensity data
146 collections are summarized in Table S2. The diffraction patterns were indexed and intensities
147 integrated using the X-area 1.72 software (Stoe & Cie GmbH). Integrated intensities were corrected
148 for absorption effects, through DAC components and sample, by using the *ABSORB* code (Angel and
149 Gonzales-Platas 2013).

150 Crystal structures were refined with *JANA2006* suite (Petricek et al. 2014) using neutral
151 atomic scattering factors of Cs, K, Mg, Fe, B, Be, Si, and O according to the International Tables for
152 Crystallography (Prince 2006). The structure refinements were performed against F using the
153 structure model previously reported by Palke et al. (2021). Secondary isotropic extinction effect was
154 corrected according to the formalism of Becker and Coppens (1974), implemented in *JANA2006*. Due
155 to ambiguity in the true symmetry, as discussed by Palke et al. (2021), various approaches for
156 structure refinements were carried out in space groups $P6/mcc$ (192), $P\bar{3}1c$ (163) and $P\bar{3}c1$ (165).
157 The structure solution of the data at 6.50 GPa was performed using the *SUPERFLIP* computer
158 program (Palatinus and Chapuis 2007), applying the charge-flipping algorithm. Statistical parameters
159 and other details pertaining to the final refinements are given in Table S2, the atomic positions and
160 displacement parameters are listed in Table S3 and other relevant structural parameters in Table S4
161 (and in the CIF).

162

163

164 **Results**

165 ***High-pressure Raman spectra***

166 The reference spectrum at 0.0001 GPa is practically identical to the original Raman spectrum
167 described by Palke et al. (2021), featuring the same resonance bands at corresponding bands positions
168 (at $\sim 1085\text{ cm}^{-1}$, $\sim 1040\text{ cm}^{-1}$, $\sim 692\text{ cm}^{-1}$, $\sim 624\text{ cm}^{-1}$, $\sim 505\text{ cm}^{-1}$, $\sim 430\text{ cm}^{-1}$, $\sim 405\text{ cm}^{-1}$, $\sim 260\text{ cm}^{-1}$ and
169 $\sim 225\text{ cm}^{-1}$ at ambient conditions, cf. Figure 1). With reference to the existing spectral analyses on
170 beryl, pezzottaite and related mineral structures, the observed bands can be assigned to vibration
171 modes of the Si_6O_{18} rings with or without involvement of neighboring tetrahedral and octahedral units
172 (Hofmeister et al. 1987; Kim et al. 1995; Moroz et al. 2000; Lambruschi et al. 2014; Ende et al. 2021).

173 The Raman spectrum at ambient conditions exhibits no characteristic Raman band in the low-
174 frequency regime between the system limit (50 cm^{-1}) and 200 cm^{-1} Raman shift. Such a vibrational
175 band was found for pezzottaite around 111 cm^{-1} and was attributed to Cs-O vibrations (Ende et al.
176 2021). Nevertheless, it is noticeable that in the range that is typical for the highly coordinated Cs and
177 other large alkali atoms, the spectral background increases significantly towards the lowest
178 frequencies at the system limit, an observation that has not been reported by Palke et al. (2021), since
179 their measurements were made in the $200\text{--}2000\text{ cm}^{-1}$ frequency range. However, at non-ambient
180 pressures, the maximum corresponding to an intense band located below the 50 cm^{-1} limit becomes
181 visible due to the pressure-induced blueshift (Figure 1). This supposed maximum becomes
182 recognizable above $\sim 3\text{ GPa}$, but it should probably also exist at lower pressures and cannot be
183 detected due to the lower spectral limit of the Raman spectrometer. While only one clear band can be
184 seen in all spectra up to about 3.5 GPa , the appearance of two further bands located at $\sim 80\text{ cm}^{-1}$ and
185 $\sim 120\text{ cm}^{-1}$ can be observed in all spectra above $\sim 4\text{ GPa}$. This indicates changes related to the
186 coordination of the Cs site, involving either point symmetry changes or the occurrence of individual
187 Cs sites. It is remarkable that the transition described for pezzottaite also resulted in significant
188 changes in the low-frequency spectral range near the 111 cm^{-1} band, as new bands assigned to the Cs
189 atoms evolved with the reported transition (Figure 1).

190 Although the apparent changes described at 4 GPa are the most striking in the entire Raman
191 spectrum, there are further indications of changes in other spectral regions that give a clear indication
192 of the presence of a phase transformation. A slight change in the value of pressure dependence of the
193 band position $\partial\nu/\partial P$ is evident for several bands (e.g., for $\nu(1040)$ and $\nu(1085)$ in Figure 2). A
194 somewhat clearer indication is the splitting of $\nu(1084)$, which is easily recognizable from $\sim 4\text{ GPa}$
195 with two clearly separable maxima and, assigned as Si-O stretching mode, also indicates changes in
196 point symmetry or symmetry of sites related to the Si atoms. Another clear indication are the changes

197 in the relative intensities of individual bands, *e.g.* the intensity inversion related to the bands at ~405
198 cm^{-1} and ~340-360 cm^{-1} . In summary, it can be stated that many individual subtle spectral changes
199 are associated with the critical pressure at around 4 GPa. The spectra at pressure below and above
200 this transition point show an overall degree of similarity, so that one can assume that the structural
201 topology is, overall, preserved, and in this case only changes in the overarching symmetry are likely
202 to occur. It should be added that the same changes can be observed in both compression and
203 decompression, without significant hysteresis concerning the critical transition pressure.

204

205 *Lattice properties and static elasticity*

206 The unit-cell parameters measured at 16 different pressures up to ~8.4 GPa are summarized
207 in Table S5. The least-squares refinements of base vectors were performed in a first step with
208 symmetry-unconstrained parameters in a triclinic setting, in order to determine possible pseudo-
209 symmetries due to symmetry breaking. The symmetry-unconstrained refinements confirmed the
210 hexagonal setting of base vectors with a being equal to b within the experimental uncertainties, and
211 the angles α , β , and γ showing values close to 90° , 90° and 120° , respectively.

212 The P dependency of unit-cell parameters (Figure 3) reveals a compressional anisotropy with
213 the structure being ~10 % less compressible along the c -axis than along the a -axis (Table 1), following
214 a pattern of anisotropy similar to that of pezzottaite but different from that of beryl or cordierite
215 (Miletich et al. 2014a,b; Scheidl et al. 2014; Fan et al. 2015; O'Bannon and Williams 2016; Ende et
216 al. 2021). An obvious change in the compression behavior can be observed from the critical pressure
217 of ~4 GPa, as described in the high-pressure Raman spectroscopic investigations. Above the critical
218 transition pressure, a significantly higher compressibility is noticeable both in the bulk and in the
219 individual crystallographic axis directions without the occurrence of a significant discontinuity,
220 which would be typical for a first-order phase transition. Fitting a Birch-Murnaghan EoS (Birch 1947)
221 to the experimental data (Figure 3), the pressure derivatives of the moduli K_0 (for volume) and M_0
222 (axial) show negative values for the data ≤ 3.55 GPa, *i.e.* $M' = \partial M_0 / \partial P \approx -8$ for the c -axis, and even
223 negative values for the volume with $K' = \partial K_0 / \partial P \approx -2 \pm 3$. The occurrence of axial negative values
224 has been previously reported for irradiated and non-irradiated cordierite (Miletich et al. 2014a,b;
225 Scheidl et al. 2014), and pezzottaite (Ende et al. 2021), while studies on beryl itself did not report any
226 anomalous behavior (Fan et al. 2015). Structural instabilities have been reported for isostructural
227 materials associated with remarkable elastic-softening behavior, which can be interpreted as a
228 precursor effect of an impending transition in beryl-type phases (Miletich et al. 2014a,b; Scheidl et
229 al. 2014; Ende et al. 2021).

230 Fits according to Birch-Murnaghan EoS with constraints on K' reveal bulk moduli of 148 ± 3
231 GPa (with K' set to 0) and 75.5 ± 0.9 GPa (with K' set to 4) for the respective low- and high-pressure
232 form (Table 1). The aforementioned fixed values of the pressure derivative (*i.e.*, K' set to 0 for the
233 low- P form and to 4 for the high- P form) provided the best figures of merit of the EoS fits. Referring
234 to the Anderson-Anderson relationship (Anderson and Anderson 1970), the bulk modulus of the low-
235 P form is very similar to that reported for pezzottaite ($K_0 = 152$ GPa at $V/Z = 341.3 \text{ \AA}^3$ per formula
236 unit Z), and plots between those of beryl [$K_0 = 180$ GPa, $V_0/Z = 337.7 \text{ \AA}^3$ p.f.u. (Fan et al. 2015)]
237 and cordierite [$K_0 = 131$ GPa, $V_0/Z = 387.9 \text{ \AA}^3$ p.f.u. (Miletich et al. 2014a)]. In contrast, the high-
238 pressure form of johnkoivulaite is significantly softer as expressed by the parameters obtained for the
239 fit to the 2nd order Birch-Murnaghan EoS ($K'=4$), for which the bulk modulus is only 75.5 ± 0.9 GPa
240 at an extrapolated $V_0/Z = 358.5 \text{ \AA}^3$ p.f.u. (Table 1). Only by simply comparing the volume-related
241 lattice elasticities can it be determined that the low- P form of johnkoivulaite and pezzottaite, despite
242 crystallographic differences in terms of symmetry, are similar and behave analogously to the other
243 beryl structures with respect to their compression properties. From these points of view alone, the
244 high- P form of johnkoivulaite is outstanding and so far unique, since it deviates significantly from
245 the trend line corresponding to the Anderson-Anderson relationship.

246 The determination of the point of intersection from the two parameterized equations of state
247 allows the critical transition pressure to be bracketed with a value of 4.13 ± 0.07 GPa, taking into
248 account the uncertainties determined from the fits.

249

250 ***Re-evaluating the crystal structure at ambient conditions***

251 At ambient conditions, diffraction data were successfully indexed with the hexagonal unit-
252 cell as reported by Palke et al. (2021) (*i.e.*, $a \sim 9.47$ and $c \sim 9.05 \text{ \AA}$), with reflection conditions
253 consistent with the space group $P6/mcc$ (192). Cs *vs.* K fraction at the Cs site, Mg *vs.* Fe fraction at
254 the Mg site, and B *vs.* Be fraction at the Be site were refined, providing values in good agreement
255 with those previously reported by Palke et al. (2021). Convergence was rapidly archived after a few
256 cycles of refinement, without any significant correlation among the refined variables or anomalous
257 residuals in the difference-Fourier function of the electron density. Any of the conventional
258 parameters validating the structure refinement in $P6/mcc$ (*i.e.*, $R(F)$ and $wR(F)$ for $I_o > 3\sigma(I_o)$ are,
259 respectively, 1.36% and 2.09%, Table S2 and CIF) leaves no doubt about the correctness of the
260 structure determination and the previous choice of the space group (Palke et al. 2021). In addition, all
261 anisotropic displacement ellipsoids were positive definite. The most anisotropic ones are those of the
262 $O1$ and $O2$ sites, as already reported by Palke et al. (2021), which appears to be a common feature of

263 the bridging oxygen atoms in cyclosilicates with corner-sharing polyhedra that confine a channel
264 [e.g., beryl (Gatta et al. 2006); cordierite (Cohen et al. 1977); pezzottaite (Gatta et al. 2012)].

265 Nevertheless, an ordering of the Be and B cations, which lie at the $6f$ site in $P6/mcc$, is to be
266 expected, theoretically in tandem with a lowering of symmetry, corresponding to a subgroup
267 symmetry of the parental $P6/mcc$. On the other hand, the real differences between the two X-ray
268 scattering curves of Be and B are so marginal that, regardless of their ordering state, the relevant
269 structure factors have values that are insignificantly different and, therefore, possible differences
270 simply cannot be detected. An apparent analogy to pezzottaite regarding the cation order on the
271 respective T site [i.e., $\sim 2/3$ Be and $\sim 1/3$ Li, as shown by Yakubovich et al. (2009), Gatta et al. (2012),
272 and Ende et al. (2021)] suggests the existence of a comparable R -centered superstructure (i.e., $R\bar{3}c$
273 (167), $a = \sim 15.9$ and $c = \sim 27.8$ Å, corresponding to $a_{\text{pezzottaite}} = a_{\text{beryl}} \cdot \sqrt{3}$, $c_{\text{pezzottaite}} = 3 \cdot c_{\text{beryl}}$). Careful
274 inspection on the reciprocal space, as reconstructed from the recorded frames, did not provide any
275 evidence for the existence of comparable superstructure reflections, either in terms of triplication of
276 the c -axis or in terms of significant intensities at the reciprocal lattice points located on $(3n+1)/3$ or
277 $(3n+2)/3$ relative to the base vectors of the beryl-type subcell.

278 Careful inspection on the reflection statistics shows, for the measurement at 0.0001 GPa, three
279 forbidden reflections with $I_o > 3\sigma(I_o)$ for the reflection class $h0l$, hinting at the existence of a c -glide
280 plane parallel to $(h0l)$. Any violation of the zonal extinctions in the reflection classes $h0l$ and hhl ,
281 attributed to the existence of the two c -glide mirror planes, cannot be confirmed without doubt due to
282 the low number of violating reflections and low values for the observed intensities as expressed by
283 the $I/\sigma(I)$ values. Due to the excellent crystal quality with only minor lattice mosaicity, there is a
284 certain possibility that multiple diffraction (in the sense of a Renninger effect) can also be responsible
285 for the subtle violation of the extinction conditions. Based on a possible direct group-subgroup
286 relationship, the trigonal space group $P\bar{3}1c$ (163) or even merohedral twinning following $Cccm$ (66)
287 symmetry might be likely. Attempts to refine the data sets collected within this study did not provide
288 any significant evidence for alternative space-group symmetries. Again, the existence of
289 superstructure reflections can be ruled out and, moreover, none of the available measurements could
290 detect any of the diffuse scattering as described for pezzottaite (Ende et al. 2021), which seems
291 plausible due to the higher degree of order inside the channels due to the lower Cs deficiency and the
292 lack of significant Na contents.

293
294

295 *Determination of the high-pressure crystal structure*

296 Diffraction data collected at 6.50 ± 0.05 GPa showed that the high-*P* polymorph is metrically
297 trigonal based on a hexagonal setting, but with different base vectors compared to the low-*P*
298 polymorph, corresponding to $a \sim 16.13$ Å and $c \sim 8.85$ Å. The metrical relationship between the unit-
299 cells of the different polymorphs is shown in Figure 4, and explains the appearance of superstructure
300 reflections in the reciprocal space. In Figure 5, relevant sections of reconstructed reciprocal space
301 allow a direct comparison of the diffraction data obtained at 1.65 and 6.50 GPa. In order to define the
302 real symmetry of the high-*P* polymorph, a series of tests have been performed considering the
303 possible space groups generated by group-subgroup relationships with the parental one *P6/mcc*. The
304 best figure of merit was obtained with the point groups $\bar{3}m1$ and $\bar{3}$. The space group $P\bar{3}c1$ (165) was
305 finally selected, with twinning of two individuals metrically related by (0 1 0, -1 -1 0, 0 0 1) and a
306 twin ratio of 0.5:0.5. A lower symmetry, with space group $P\bar{3}$ (147) cannot be ruled out, but a stable
307 structure refinement was not possible due to the high number of variables.

308 Compared to the low-*P* polymorph, symmetry lowering of the high-*P* one leads to a structural
309 model with two independent (Cs+K) sites (*i.e.*, *Cs1* and *Cs2*), two independent (Mg+Fe) sites (*i.e.*,
310 *Mg1* and *Mg2*), three unique sites fully populated by Si (*i.e.*, *Si1*, *Si2* and *Si3*), nine unique sites
311 occupied by O (*i.e.*, *O1a-O1f* and *O2a-O2c*) and two (B+Be) sites (*i.e.*, *Be1* and *Be2*) (Table S3 and
312 CIF). The fraction of Cs and K at the *Cs1* and *Cs2*, along with that of Mg and Fe at *Mg1* and *Mg2*,
313 were successfully refined (with an excellent agreement to the refinement at room conditions, Table
314 S3 and CIF); the fraction of B and Be at the *Be1* and *Be2* sites were fixed to 1/3 and 2/3, respectively.
315 While at 0.0001 GPa the structure was modelled with anisotropic displacement parameters for all the
316 atomic sites, at 1.65 GPa only the atomic sites with greater X-ray scattering factors (populated by
317 Cs/K, Si and O) were refined with anisotropic displacement parameters, and at 6.50 GPa only the *Cs1*
318 and *Cs2* sites were modelled anisotropically for the trigonal structure model. Despite the increase of
319 the refined parameters of the high-*P* polymorph, the structure refinement was conducted with a
320 reasonable ratio between the number of observed structure factors versus the number of refined
321 parameters (~ 9.8) (Table S2 and CIF). At the end of the refinement [with $R(F_{\text{obs}}) = 0.0560$, 55 refined
322 parameters and 540 observed reflections], converge was achieved, and the variance-covariance matrix
323 showed no significant correlation between the refined parameters. The highest/lowest residuals in the
324 difference-Fourier synthesis of the electron density (*i.e.*, $\pm 2.5 e^{-\text{Å}^{-3}}$) are due to substantial local
325 disorder in the population of the *Cs1* and *Cs2* sites, along [0001].

326 The resulting interpolyhedral bond distances are presented in Table S4. Comparing the
327 structures in $P6/mcc$ and $P\bar{3}c1$, it can be seen that neither the bonding topology nor the polyhedra
328 themselves within the framework undergo significant changes. Bond distances show insignificant
329 variations and the Si , Be (=Be,B), and Mg (=Mg,Fe) polyhedra can be considered as more or less rigid
330 units. The same applies to the coordination environment of the Cs atoms, which are hosted on two
331 independent sites, with the 12-fold coordination split into 6+6 or 4x3 Cs-O bonds. The most important
332 aspect of changes relates to the symmetry reduction of the point symmetries of the special sites of all
333 cations and of $O2$. This concerns in particular: Cs (Wyckoff site $2a$, point symmetry 622)
334 transforming into $Cs1$ ($2a$, 32.) and $Cs2$ ($4d$, 3.); Si ($12l$, $m..$) into $Si1$ + $Si2$ + $Si3$ (each 12g, 1); Mg
335 ($4c$, 3.2) into $Mg1$ ($6f$, .2.) + $Mg2$ ($6f$, .2.), Be ($6f$, 222) into $Be1$ (12g, 1) + $Be2$ ($6f$, .2.), and $O2$ ($12l$,
336 $m..$) into $O2a$ + $O2b$ + $O2c$ (each 12g, 1). The degrees of freedom associated with these symmetry
337 reductions also allow the structure to relax with atomic shifts that were previously not permitted as
338 due to symmetry constraints. The only recognizable differences relate to displacive deformations of
339 the framework, which are expressed in individual inter-polyhedral bond angles. The most prominent
340 distortion concerns the ring elements, which no longer follow the strict hexagonal symmetry but adopt
341 a (di)trigonal arrangement (Figure 6).

342

343 ***Mechanism of the pressure-induced phase transition***

344 The evolution of the unit-cell volume of johnkoivulaite with P (even considering a normalised
345 volume in order to account for the new metrics of the high- P polymorph) shows that the P -induced
346 transition at ~4 GPa does not imply any remarkable discontinuity. A phase transition without any
347 volume discontinuity can be considered as to be a second-order (or a tricritical) transformation. An
348 isosymmetric phase transition would have been expected to be first-order in character (e.g., Christy
349 1995). In this light, a change of symmetry is associated with the transition from the low- P to the high-
350 P polymorph of johnkoivulaite. The symmetry breaking associated with the $P6/mcc$ -to- $P\bar{3}c1$
351 transition determines the change of the lattice periodicity within the lattice-plane direction
352 perpendicular to the c -axis. The related triplication of the unit-cell volume of the high- P polymorph
353 can be easily understood considering the splitting of the parental Cs site (at 0,0,1/4) into two
354 independent sites, i.e., $Cs1$ (at 0,0,1/4) and $Cs2$ (at 2/3,1/3,0.246). This also goes hand in hand with
355 the observed changes in the Raman spectra, where there are corresponding splittings in the range of
356 the low-frequency bands that can be assigned to the Cs polyhedra, which in turn can be attributed to
357 the lowered point symmetry and the distribution of Cs atoms on two independent sites.

358 The symmetry lowering of the high- P polymorph, with a consequent increase of the degrees
359 of freedom of structural deformation, allows a higher distortion of the coordination polyhedra of the

360 high-*P* polymorph, as can be deduced by the intra-polyhedral bond distances and angles (Table S4
361 and CIF). However, a clear picture of the distortion is partially hindered by the lower quality of the
362 post-transition intensity data set and, then, of the structure refinement, with a general increase of the
363 estimated standard deviation on lengths and angles. A pronounced distortion is observed only for the
364 *Bel*-tetrahedron, but this can also be the effect of a more difficult detection of low scatterers (*i.e.*, B,
365 Be) from the high-*P* dataset. As johnkoivulaite contains crystallographic sites with a multi-element
366 population (*i.e.*, Cs+K, Mg+Fe, B+Be); it is presumable that a phase transition, aimed to rearrange
367 the structure with an ordered distribution of the elements in distinctive sites, occurs. However, in this
368 case, the high-*P* polymorph appears to preserve the disorder. In fact, a potential Cs vs. K ordering
369 into the [0001] channel would lead to a high-*P* polymorph with a drastically longer *c* axis (as Cs/K ~
370 4/1), but johnkoivulaite does not show such a behavior. Similar consideration could be extended to
371 octahedral or tetrahedral sites with multi-element populations.

372 Diffusion-related ordering does not seem to drive the phase transition at high-pressure, which
373 is not plausible from an energetic point of view, considering that changes occur under isothermal
374 conditions. Furthermore, a comparative analysis of the high-*P* behavior of other cyclosilicates [*e.g.*,
375 beryl (Prencipe et al. 2011; O'Bannon and Williams 2016); pezzottaite (Ende et al. 2021); cordierite
376 (Miletich et al. 2014a,b; Scheidl et al. 2014; Finkelstein et al. 2015)] show that all of them experience
377 *P*-induced phase transitions towards lower symmetry. These transitions are driven by displacive
378 deformation within structural building blocks, which exhibit higher degrees of freedom associated
379 with the loss of local symmetry elements. This also applies, in general, to other ring silicates, such as
380 benitoite, BaTiSi₃O₉ (Hejny et al. 2012), which undergoes a similar transition pathway in a displacive
381 second-order phase transition, with the high-pressure polymorph being more compressible than the
382 low-pressure form. In a comparable way, a superstructure is also formed with the phase transition.

383 The noticeable changes for the cations with the highest coordination are, therefore, only a
384 consequence of the fact that these large cations, such as Cs here in the johnkoivulaite, have the
385 greatest flexibility with regard to steric-geometric adaptations of the coordination polyhedron. Even
386 in the high-*P* polymorph of johnkoivulaite, the new sites have a different bonding scheme showing a
387 6+6 coordination for *Cs1* (6x ~3.43 Å, 6x ~3.35 Å), whereas the *Cs2* site shows a 3+3+3+3 bonding
388 geometry (max: ~3.55 Å, min: ~3.14 Å) (Table S4 and CIF). It compares to a regular 12-fold
389 coordination in the parental configuration of the low-*P* polymorph (12x *Cs-O2*, with bond length of
390 ~3.40 Å at 0.0001 GPa and ~3.39 at 1.65 GPa) (Table S4 and CIF). Ultimately, however, the change
391 in the channels seems to be only a consequence of the optimization of the framework's compression
392 mechanism, which, in turn, drives the change of symmetry.

393

394

395 Discussion and Implications

396 The high-pressure form of johnkoivulaite is a new phase with respect to its crystallographic
397 structure, unique among all representatives with respect to the space group at the given lattice
398 periodicity ($P\bar{3}c1$, $a = a_{\text{beryl}} \cdot \sqrt{3}$, $c = c_{\text{beryl}}$). Trigonal superstructures derived from the aristotype beryl
399 subcell occur, so far, only in Cs-stuffed frameworks, which means that they have been exclusively
400 described for pezzottaite and HP-johnkoivulaite. Despite the stoichiometric analogies, *i.e.*, the
401 substitution of one third of the Be atoms by Li or B and the associated charge compensation by
402 additional Cs ions within the [0001]-channel, the two structures follow fundamentally different
403 ordering schemes in terms of lattice periodicities and space groups. The compression behavior of the
404 trigonal high-pressure form determined in this study is also unique compared to all other phases
405 whose structure is derived from the beryl aristotype. HP-johnkoivulaite shows about twice the
406 compression ($K_0 = \sim 76$ GPa) compared to all topologically isostructural polymorphs, while all other
407 structures are significantly stiffer, thus exhibiting compression modules that range from ~ 131 to ~ 180
408 GPa.

409 Our study shows that the phase transformation observed has all the properties of a second-
410 order transition, which is clearly displacive. While the symmetry of the high-pressure phase can be
411 determined unequivocally, the theoretical group-subgroup relationships raise doubts about the
412 correctness of the $P6/mcc$ symmetry of the low- P polymorph. With respect to group-subgroup
413 relationship, one can notice that $P\bar{3}c1$ with $a' = a\sqrt{3}$ and $c' = c$ is not a maximal subgroup and it would
414 involve an intermediate $P\bar{3}1c$ (with $a' = a$ and $c' = c$) step. The intermediate $P\bar{3}1c$ is a
415 *translationsgleiche* t_2 subgroup (index 2) of $P6/mcc$, while the $P\bar{3}1c$ to $P\bar{3}c1$ follows a *non-*
416 *translationsgleiche* isomorphic i_3 group-subgroup relation (index 3), with the observed changes in
417 the base-vector setting that involve a triplication of the unit-cell volume. The possible observation of
418 weak-intensity forbidden reflections in the $h0l$ and hhl reflection classes might be indicative of the
419 supposed non-hexagonal symmetry and that the hexagonal beryl-type structure of the low- P phase
420 represents only an average structure. However, we cannot exclude that the P -induced $P6/mcc$ -to-
421 $P\bar{3}c1$ phase transition is actually a weakly first-order transformation, and that the discontinuity in the
422 P vs. V path is not so pronounced to be detected. Similarly, we cannot exclude the possibility that a
423 transient step occurs between the $P6/mcc$ and $P\bar{3}c1$ polymorphs, with an additional polymorph with
424 a very narrow stability field in pressure, whose symmetry and metrical relationships can be consistent
425 with the low- and high-polymorphs observed here in terms of group-subgroup relationship.

14

426 The findings of our investigations on only the second example of a Cs-stuffed beryl structure
427 suggest an influence of the channel fillings on the stability of the framework under pressure. In
428 contrast to frameworks that are either empty or only partially occupied by intercalated molecules on
429 partially occupied sites, the large alkali atoms seem to play an important role on the stabilization of
430 the framework, as observed in other open-framework materials [i.e., the so-called “pillar effect”
431 (Gatta et al. 2018)]. These relatively large extra framework components prevent a pressure-induced
432 collapse of the channels, as has been described for the structures of beryl and cordierite, where the
433 formation of modulated structures or highly twinned microstructures of low-symmetrical crystal
434 domains with corresponding deformation of the channel geometries takes place. As also seen with
435 pezzottaite, the incorporation of the Cs atoms seems to bring about a stabilization of the channels
436 with regard to their symmetry, to counteract an elliptical deformation, and thus also to be responsible
437 for maintaining a highly symmetrical framework structure. This is an important prerequisite if one
438 actually wants to consider the beryl-type structure as a host phase for radiogenic Cs-137 and also
439 wants to avoid instability under mechanical stress for such a stable host phase. These aspects of
440 structural stability are an important prerequisite for being able to guarantee the immobility of isotopes
441 with regard to possible technological use.

442

443 **Acknowledgements**

444 We are grateful to Andreas Wagner (IfMK, University of Vienna) for all the effort in the sample
445 preparation. We thank University of Vienna for financial support within the scope of the grants
446 BE532003 and IP532022 and the Italian Ministry of Education (MIUR) through the project
447 “PRIN2017 - Mineral reactivity, a key to understand large-scale processes” (2017L83S77). G.
448 Bromiley, an anonymous Reviewer and the Structures Editor Team are warmly thanked for the
449 revision of the manuscript.

450

451

452 **References**

- 453 Anderson, D.L., and Anderson, O.L. (1970) Brief report: The bulk modulus-volume relationship for
454 oxides. *Journal of Geophysical Research*, 75, 3494–3500.
- 455 Angel, R.J., Allan, D.R., Miletich, R., and Finger, L.W. (1997) The Use of Quartz as an Internal
456 Pressure Standard in High-Pressure Crystallography. *Journal of Applied Crystallography*, 30, 461–
457 466.

- 458 Angel, R.J., and Finger, L.W. (2011) SINGLE : a program to control single-crystal diffractometers.
459 Journal of Applied Crystallography, 44, 247–251.
- 460 Angel, R., and Gonzalez-Platas, J. (2013) *ABSORB-7* and *ABSORB-GUI* for single-crystal absorption
461 corrections. Journal of Applied Crystallography, 46, 252–254.
- 462 Artioli, G., Rinaldi, R., Ståhl, K., and Zanazzi, P.F. (1993) Structure refinement of beryl single-crystal
463 neutron and X-ray diffraction. American Mineralogist, 78, 762–768.
- 464 Armbruster, T. (1985a) Crystal structure refinement, Si,Al-ordering, and twinning in
465 “pseudohexagonal” Mg-cordierites. Neues Jahrbuch für Mineralogie Monatshefte, 6, 255–267.
- 466 Armbruster, T. (1985b) Ar, N₂, and CO₂ in the structural cavities of cordierite, and optical and X-ray
467 single-crystal study. Physics and Chemistry of Minerals, 12, 233–245.
- 468 Armbruster, T. (1986) Role of Na in the structure of low-cordierite: A single-crystal X-ray study.
469 American Mineralogist, 71, 746–757.
- 470 Armbruster, T., Libowitzky, E., Auernhammer, M., Bauerhansl, P., Hoffmann, C., Irran, E., Kurka,
471 A., Rosenstingl, H., and Diamond, L. (1995) Crystal chemistry and optics of bazzite from Furka-
472 basistunnel (Switzerland). Mineralogy and Petrology, 52, 113–126.
- 473 Barton, M.D., and Young, S. (2002) Non-pegmatitic Deposits of Beryllium: Mineralogy, Geology,
474 Phase Equilibria and Origin. Reviews in Mineralogy and Geochemistry, 50, 591–691.
- 475 Birch, F. (1947) Finite elastic strain of cubic crystals. Physical Review, 71, 809–824.
- 476 Bragg W.L. & West, J. (1926) The structure of beryl, Be₃Al₂Si₆O₁₈. Proceedings of the Royal Society
477 of London - Series A, Mathematical and Physical Sciences, 111, 691–714.
- 478 Cohen, J.P., Ross, F.K., and Gibbs, G.V. (1977) An X-ray and neutron diffraction study of hydrous
479 low cordierite. American Mineralogist, 62, 67–78.
- 480 Christy, A. (1995) Isosymmetric Structural Phase Transitions: Phenomenology and Examples. Acta
481 Crystallographica, B51, 753–757
- 482 Becker, P. J., and Coppens, P. (1974) Extinction within the limit of validity of the Darwin transfer
483 equations. I. General formalism for primary and secondary extinction and their applications to
484 spherical crystals. Acta Crystallographica, A30, 129–147.
- 485 Charoy, B., De Donato, P., Barres, O., and Pinto-Coelho, C. (1996) Channel occupancy in an alkali-
486 poor beryl from Serra Branca (Goias, Brazil): Spectroscopic characterization. American
487 Mineralogist, 81, 395–403.

- 488 Daniels, P., Wunder, B., Sahl, K., and Schreyer, W. (1994) Changing lattice metrics of synthetic
489 cordierites: the metastable hexagonal to orthorhombic transformation sequence during isothermal
490 annealing. *European Journal of Mineralogy*, 6, 323-335.
- 491 Deer, W.A., Howie, R.A., and Zussman, J. (1992) An introduction to the rock-forming minerals. 2nd
492 edition, Longman Scientific & Technical, London, UK, 696 p.
- 493 Della Ventura, G., Rossi, P., Parodi, G.C., Mottana, A., Raudsepp, M., and Prencipe, M. (2000)
494 Stoppaniite, $(\text{Fe,Al,Mg})_4(\text{Be}_6\text{Si}_{12}\text{O}_{36}) \cdot (\text{H}_2\text{O})_2(\text{Na},\square)$ a new mineral of the beryl group from Latium
495 (Italy). *European Journal of Mineralogy*, 12, 121–127.
- 496 Ende, M., Gatta, G.D., Lotti, P., Grandtner, A., and Miletich, R. (2021) $\text{Cs}(\text{Be}_2\text{Li})\text{Al}_2\text{Si}_6\text{O}_{18}$, a
497 cesium-stuffed host-guest structure, and its structure-property variations with temperature and
498 pressure. *Journal of Solid State Chemistry*, 293, 121841.
- 499 Fan, D., Xu, J., Kuang, Y., Li, X., Li, Y., and Xie, H. (2015) Compressibility and equation of state of
500 beryl ($\text{Be}_3\text{Al}_2\text{Si}_6\text{O}_{18}$) by using a diamond anvil cell and in situ synchrotron X-ray diffraction.
501 *Physics and Chemistry of Minerals*, 42, 529–539.
- 502 Ferraris, G., Prencipe, M., and Rossi, P. (1998) Stoppaniite, a new member of the beryl group: crystal
503 structure and crystal-chemical implications. *European Journal of Mineralogy*, 10, 491-496.
- 504 Finkelstein, G., Dera, P., and Duffy, T. (2015) High-pressure phases of cordierite from single-crystal
505 X-ray diffraction to 15 GPa. *American Mineralogist*, 100, 1821-1833.
- 506 García-Moreno, O., Corretgé, L.G., and Castro, A. (2007) Processes of assimilation in the genesis of
507 cordierite leucomonzogranites from the Iberian Massif: a short review. *Canadian Mineralogist*, 45,
508 71–85.
- 509 Gatta, G.D., Nestola, F., Bromiley, G.D., and Mattauch, S. (2006) The real topological configuration
510 of the extra-framework content in alkali-poor beryl: a multi-methodological study. *American*
511 *Mineralogist*, 91, 29-34.
- 512 Gatta, G.D., Adamo, I., Meven, M., and Lambruschi, E. (2012) A single-crystal neutron and X-ray
513 diffraction study of pezzottaite, $\text{Cs}(\text{Be}_2\text{Li})\text{Al}_2\text{Si}_6\text{O}_{18}$. *Physics and Chemistry of Minerals*, 39, 829–
514 840.
- 515 Gatta, G.D., Lotti, P., and Tabacchi, G. (2018) The effect of pressure on open-framework silicates:
516 elastic behaviour and crystal–fluid interaction. *Physics and Chemistry of Minerals*, 45, 115–138.
- 517 Gibbs, G.V., Breck, D.W., and Meagher, E.P. (1968) Structural refinement of hydrous and anhydrous
518 synthetic beryl, $\text{Al}_2(\text{Be}_3\text{Si}_6)\text{O}_{18}$ and emerald, $\text{Al}_{1.9}\text{Cr}_{0.1}(\text{Be}_3\text{Si}_6)\text{O}_{18}$. *Lithos*, 1, 275–285.

- 519 Gonzalez-Platas, J., Alvaro, M., Nestola, F., and Angel, R. (2016) *EosFit7-GUI*: a new graphical
520 user interface for equation of state calculations, analyses and teaching. *Journal of Applied*
521 *Crystallography*, 49, 1377–1382.
- 522 Hejny, C., Miletich, R., Jasser, A., Schouwink, P., Crichton, W., and Kahlenberg, V. (2012) Second
523 order $P\bar{6}c2-P31c$ structural transition and structural crystallography of the cyclosilicate benitoite,
524 $BaTiSi_3O_9$, at high pressure. *American Mineralogist*, 97, 1747-1763.
- 525 Hess, P.C. (1969) The Metamorphic Paragenesis of Cordierite in Pelitic Rocks. *Contributions to*
526 *Mineralogy and Petrology*, 24, 191-207.
- 527 Hofmeister, A.M., Hoering, T.C., and Virgo, D. (1987) Vibrational spectroscopy of beryllium
528 aluminosilicates: Heat capacity calculations from band assignments. *Physics and Chemistry of*
529 *Minerals*, 14, 205–224.
- 530 Jacobsen, S.D., Holl, C.M., Adams, K.A., Fischer, R.A., Martin, E.S., Bina, C.R., Lin, J.F.,
531 Prakapenka, V.B., Kubo, A., and Dera, P. (2008) Compression of single-crystal magnesium oxide
532 to 118 GPa and a ruby pressure gauge for helium pressure media. *American Mineralogist*, 93,
533 1823–1828.
- 534 Kim, C.C., Bell, M.I., and McKeown, D.A. (1995) Vibrational analysis of beryl ($Be_3Al_2Si_6O_{18}$) and
535 its constituent ring (Si_6O_{18}). *Physica B: Condensed Matter*, 205, 193–208.
- 536 King, H.E., and Finger, L.W. (1979) Diffracted beam crystal centering and its application to high-
537 pressure crystallography. *Journal of Applied Crystallography*, 12, 374–378.
- 538 Klein, C., and Philpotts, A.R. (2012) *Earth Materials: Introduction to Mineralogy and Petrology*.
539 Cambridge University Press, UK, 552 p. (ISBN 0521761158).
- 540 Kolesov, A., and Geiger, C.A. (2000) Cordierite II. The role of CO_2 and H_2O . *American Mineralogist*,
541 85, 1265-1274.
- 542 Lambruschi, E., Gatta, G.D., Adamo, I., Bersani, D., Salvioli-Mariani, E., and Lottici, P.P. (2014)
543 Raman and structural comparison between the new gemstone pezzottaite $Cs(Be_2Li)Al_2Si_6O_{18}$ and
544 Cs-beryl. *Journal of Raman Spectroscopy*, 45, 993–999.
- 545 Malcherek, T., Domeneghetti, M.C., Tazzoli, V., Ottolini, L., McCammon, C., and Carpenter, M.A.
546 (2001) Structural properties of ferromagnesian cordierites. *American Mineralogist*, 86, 66-79.
- 547 Mashkovtsev, R.I., and Thomas, V.G. (2005) Nitrogen atoms encased in cavities within the beryl
548 structure as candidates for qubits. *Applied Magnetic Resonance*, 28, 401–409.

- 549 Miletich, R., Allan, D.R., and Kuhs, W.F. (2000) High-Pressure Single-Crystal Techniques. Reviews
550 in Mineralogy and Geochemistry, 41, 445–519.
- 551 Miletich, R., Gatta, G.D., Willi, T., Mirwald, P.W., Lotti, P., Merlini, M., Rotiroti, N., and Loerting,
552 T. (2014) Cordierite under hydrostatic compression: Anomalous elastic behavior as a precursor
553 for a pressure-induced phase transition. American Mineralogist, 99, 479-492.
- 554 Miletich, R., Scheidl, K.S., Schmitt, M., Moissl, A.P., Pippinger, T., Gatta, G.D., Schuster, B., and
555 Trautmann, C. (2014) Static elasticity of cordierite I: Effect of heavy ion irradiation on the
556 compressibility of hydrous cordierite. Physics and Chemistry of Minerals, 41, 579-591.
- 557 Moroz, I., Roth, M., Boudeulle, M., and Panczer, G. (2000) Raman microspectroscopy and
558 fluorescence of emeralds from various deposits. Journal of Raman Spectroscopy, 31, 485–490.
- 559 O'Bannon, E., and Williams, Q. (2016) Beryl-II, a high-pressure phase of beryl: Raman and
560 luminescence spectroscopy to 16.4 GPa. Physics and Chemistry of Minerals, 43, 671–687.
- 561 Palatinus, L., and Chapuis, G. (2007) SUPERFLIP—A Computer Program for the Solution of Crystal
562 Structures by Charge Flipping in Arbitrary Dimensions. Journal of Applied Crystallography, 40,
563 786-790.
- 564 Palke, A.C., Henling, L.M., Rossman, G.R., Sun, Z., Renfro, N., Kampf, A.R., Thu, K., Myo, N.,
565 Wongrawang, P., and Weeramonkhonlert, V. (2021) Johnkoivulaite, Cs(Be₂B)Mg₂Si₆O₁₈, a new
566 mineral of the beryl group from the gem deposits of Mogok, Myanmar. American Mineralogist,
567 106, 1844-1851.
- 568 Petříček, V., Dusek, M., and Palatinus, L. (2014) Crystallographic Computing System JANA2006:
569 General features. Zeitschrift für Kristallographie - Crystalline Materials, 229, 345-352.
- 570 Prencipe, M., Scanavino, I., Nestola, F., Merlini, M., Civalleri, B., Bruno, M., and Dovesi, R. (2011)
571 High-pressure thermo-elastic properties of beryl (Al₄Be₆Si₁₂O₃₆) from ab initio calculations, and
572 observations about the source of thermal expansion. Physics and Chemistry of Minerals, 38, 223–
573 239.
- 574 Prince, E. (2006) International Tables for Crystallography Volume C: Mathematical, physical and
575 chemical tables. International Union of Crystallography, Chester, UK.
- 576 Redfern, S.A.T., Salje, E.K.H., Maresch, W., and Schreyer, W. (1989) X-ray powder diffraction and
577 infrared study of the hexagonal to orthorhombic phase transition in K-bearing cordierite. American
578 Mineralogist, 74, 1293-1299.

- 579 Scheidl, K.S., Gatta, G.D., Pippinger, T., Schuster, B., Trautmann, C., and Miletich, R. (2014) Static
580 elasticity of cordierite II: effect of molecular CO₂ channel constituents on the compressibility.
581 *Physics and Chemistry of Minerals*, 41, 617-631.
- 582 Scheidl, K.S., Miletich, R., Kurnosov, A., Trots, D.M., Boffa Ballaran, T., and Angel, R.J. (2016)
583 Extending the single-crystal quartz pressure gauge up to hydrostatic pressure of 19 GPa. *Journal*
584 *of Applied Crystallography*, 49, 2129–2137.
- 585 Spear, F.S. (1993) *Metamorphic Phase Equilibria and Pressure – Temperature – Time Paths*.
586 *Monograph. Mineralogical Society of America*, Washington, D.C. (2nd printing with corrections
587 1995), 799 p., ISBN 0-939950-34-0.
- 588 Wilson, A.J.C., and Prince, E. (1999) *International Tables for Crystallography, Vol. C, 2nd ed.*,
589 *Kluwer Academic Publishers*, Dordrecht, The Netherlands.
- 590 Yakubovich, O.V., Pekov, I.V., Steele, I.M., Massa, W., and Chukanov, N.V. (2009) Alkali metals
591 in beryl and their role in the formation of derivative structural motifs: Comparative crystal
592 chemistry of vorobyevite and pezzottaite. *Crystallographic Reports*, 54, 399–412.
- 593
- 594
- 595
- 596
- 597
- 598
- 599
- 600
- 601
- 602
- 603
- 604

605 **Table 1.** Bulk moduli K_0 and axial moduli M_0 and their pressure derivatives K' and M' obtained for
 606 fits of the Birch-Murnaghan equation-of-state. For better comparability, the base vector of the beryl
 607 subcell was used for the a -axis of both polymorphic forms; volumes therefore correspond to that of
 608 the beryl subcell.

609
610

611	P -range (GPa)	EoS-type*	X_0	K_0, M_0	K', M'
612	<hr/>				
613	<i>Volume**</i>				
614	0.457-3.553	BM-3	$V_0 = 702.7(2) \text{ \AA}^3$	$K_0 = 152(7) \text{ GPa}$	$K' = -2(3)$
615	0.457-3.553	BM-3 ($K'=\text{fix}$)	$V_0 = 702.8(2) \text{ \AA}^3$	$K_0 = 148(2) \text{ GPa}$	$K' = 0$
616	4.765-8.414	BM-3	$V_0 = 721(5) \text{ \AA}^3$	$K_0 = 68(14) \text{ GPa}$	$K' = 5(3)$
617	4.765-8.414	BM-2 ($K'=4$)	$V_0 = 718.2(5) \text{ \AA}^3$	$K_0 = 75.5(9) \text{ GPa}$	$K' = 4$
618	<hr/>				
619	<i>a-axis**</i>				
620	0.457-3.553	BM-3	$a_0 = 9.4736(20) \text{ \AA}$	$M_0 = 441(43) \text{ GPa}$	$M' = 10(20)$
621	0.457-3.553	BM-3 ($M'=\text{fix}$)	$a_0 = 9.4728(10) \text{ \AA}$	$M_0 = 462(9) \text{ GPa}$	$M' = 0$
622	4.765-8.414	BM-3	$a_0 = 9.527(17) \text{ \AA}$	$M_0 = 257(48) \text{ GPa}$	$M' = 13(9)$
623	4.765-8.414	BM-2 ($M'=12$)	$a_0 = 9.525(3) \text{ \AA}$	$M_0 = 263(4) \text{ GPa}$	$M' = 12$
624	<hr/>				
625	<i>c-axis</i>				
626	0.457-3.553	BM-3	$c_0 = 9.0445(2) \text{ \AA}$	$M_0 = 423(34) \text{ GPa}$	$M' = -8(14)$
627	0.457-3.553	BM-3 ($M'=\text{fix}$)	$c_0 = 9.0444(9) \text{ \AA}$	$M_0 = 411(7) \text{ GPa}$	$M' = 0$
628	4.765-8.414	BM-3	$c_0 = 9.177(23) \text{ \AA}$	$M_0 = 131(40) \text{ GPa}$	$M' = 21(10)$
629	4.765-8.414	BM-2 ($M'=12$)	$c_0 = 9.144(3) \text{ \AA}$	$M_0 = 173(2) \text{ GPa}$	$M' = 12$
630	<hr/>				

631
632 * BM-3 = third-order Birch-Murnaghan EoS; BM-2 = second-order Birch-Murnaghan EoS

633 ** of the beryl subcell ($V_{\text{subcell}} = V_{LP\text{-phase}}$; $V_{\text{subcell}} = 1/3 V_{HP\text{-phase}}$; $a_{\text{subcell}} = a_{LP\text{-phase}}$; $a_{\text{subcell}} = 1/\sqrt{3} a_{HP\text{-phase}}$)

634
635
636

637 **Table S1 (deposited).** Experimental details of the various DAC high-pressure loadings.
 638

639 Application	Raman spectra	XRD intensities (crystal structures)	XRD lattice parameters (equation of state)
642 DAC type	ETH	ETH	ETH
643 Anvil type and culet C	BA, C=0.6 mm	BA, C=0.6 mm	BA, C=0.6 mm
644 Thickness of pre-indented gasket	83 ± 2 μm	90 ± 2 μm	105 ± 2 μm
645 Pressure-chamber diameter	225 ± 5 μm	260 ± 5 μm	270 ± 5 μm
646 Sample crystal (johnkoivulaite)	70 × 70 × 40 μm ³	220 × 130 × 40 μm ³	150 × 110 × 40 μm ³
647 XRD pressure calibrant (quartz)	-	-	90 × 55 × 40 μm ³
648 Optical pressure sensor	ruby	ruby	ruby
649 Pressure-transmitting medium	argon	4:1 methanol-ethanol	4:1 methanol-ethanol
650 Applied pressures	0.0001 to 10.19 GPa	1.65, 6.50 GPa	0.45 to 8.42 GPa

651
 652
 653
 654
 655
 656
 657

658 **Table S2 (deposited).** Experimental details of the single-crystal X-ray structure investigations
 659 (crystal data, intensity data collection, data processing and structure refinements). Statistical
 660 parameters as defined by the *JANA2006* suite (Petricek et al. 2014).
 661

662	<i>P</i> (GPa)	0.0001	1.65(6)	6.50(5)
663				
664	Unit-cell parameters	<i>a</i> = 9.470(1) Å	<i>a</i> = 9.450(1) Å	<i>a</i> = 16.130(2) Å
665		<i>c</i> = 9.050(3) Å	<i>c</i> = 9.010(3) Å	<i>c</i> = 8.850(2) Å
666		<i>V</i> = 702.9(2) Å ³	<i>V</i> = 696.8(3) Å ³	<i>V</i> = 1994.1(6) Å ³
667	Space group	<i>P</i> 6/ <i>mcc</i> (192)	<i>P</i> 6/ <i>mcc</i> (192)	<i>P</i> $\bar{3}$ <i>c</i> 1 (165)
668	<i>Z</i> [Cs(Be ₂ B)Mg ₂ Si ₆ O ₁₈]	2	2	6
669				
670	Scans	$\omega = 0.5^\circ$	$\omega = 0.5^\circ$	$\omega = 0.5^\circ$
671	$\sin\theta/\lambda$	$\leq 0.939 \text{ \AA}^{-1}$	$\leq 0.799 \text{ \AA}^{-1}$	$\leq 0.812 \text{ \AA}^{-1}$
672		$-17 \leq h \leq +17$	$9 \leq h \leq +9$	$-20 \leq h \leq +16$
673		$-17 \leq k \leq +10$	$-5 \leq k \leq +6$	$-20 \leq k \leq +24$
674		$-16 \leq l \leq +16$	$-13 \leq l \leq +9$	$-13 \leq l \leq +8$
675	Measured reflections	56397	2517	7907
676	Unique refl. $I_o > 0\sigma(I_o)$	859	390	1763
677	Unique refl. $I_o > 3\sigma(I_o)$	785	284	540
678				
679	Refined parameters	33	30	55
680	<i>R</i> _{eq}	0.0297	0.065	0.0957
681	<i>R</i> (<i>F</i>) with $I_o > 3\sigma(I_o)$	0.0136	0.0441	0.0560
682	<i>R</i> (<i>F</i>) with $I_o > 0\sigma(I_o)$	0.0157	0.0698	0.2607
683	<i>wR</i> (<i>F</i>) with $I_o > 3\sigma(I_o)$	0.0209	0.0518	0.0448
684	<i>wR</i> (<i>F</i>) with $I_o > 0\sigma(I_o)$	0.0211	0.0528	0.0534
685	Residuals (<i>e</i> /Å ³)	-0.30, +0.65	-1.19, +1.15	-2.59, +2.45
686				

687
 688
 689

690 **Table S3 (deposited).** Fractional atomic coordinates and atomic displacement parameters (U^{ij} , Å²).
 691
 692

0.0001 GPa	s.o.f	x	y	z	Ueq or Uiso	
Cs	0.808(2) Cs, 0.192(2) K	0	0	1/4	0.02399(6)	
Si	1	0.62459(2)	0.72092(2)	1/2	0.00516(6)	
Mg	0.860(4) Mg, 0.140(4) Fe	1/3	2/3	3/4	0.00727(11)	
Be	0.72(7) Be, 0.28(7) B	1/2	1/2	3/4	0.0059(4)	
O1	1	0.51954(5)	0.64490(5)	0.64777(5)	0.01248(12)	
O2	1	0.78428(7)	0.70078(8)	1/2	0.01390(17)	
	U^{11}	U^{22}	U^{33}	U^{12}	U^{13}	U^{23}
Cs	0.02764(7)	0.02764(7)	0.01669(7)	0.01382(4)	0	0
Si	0.00464(8)	0.00434(8)	0.00648(8)	0.00222(6)	0	0
Be	0.0062(5)	0.0062(5)	0.0057(5)	0.0034(4)	0	0
Mg	0.00726(15)	0.00726(15)	0.00728(17)	0.00363(7)	0	0
O1	0.01336(16)	0.01016(14)	0.01341(14)	0.00549(12)	0.00709(11)	0.00204(11)
O2	0.00865(19)	0.0129(2)	0.0241(3)	0.00827(17)	0	0
1.65 GPa	s.o.f	x	y	z	Ueq or Uiso	
Cs	0.818(6) Cs, 0.182(6) K	0	0	1/4	0.0253(5)	
Si	1	0.6243(2)	0.7209(2)	1/2	0.0079(7)	
Mg	0.857(11) Mg, 0.143(11) Fe	1/3	2/3	3/4	0.0096(9)	
Be	0.69(14) Be, 0.31(14) B	1/2	1/2	3/4	0.005(2)	
O1	1	0.5188(4)	0.6449(4)	0.6482(3)	0.0147(15)	
O2	1	0.7837(6)	0.7008(6)	1/2	0.016(2)	
	U^{11}	U^{22}	U^{33}	U^{12}	U^{13}	U^{23}
Cs	0.0294(6)	0.0294(6)	0.0171(7)	0.0147(3)	0	0
Si	0.0076(9)	0.0075(9)	0.0083(9)	0.0035(8)	0	0
O1	0.0167(18)	0.0144(19)	0.0137(18)	0.0084(15)	0.0031(14)	0.0024(14)
O2	0.013(3)	0.013(3)	0.025(3)	0.010(2)	0	0
6.50 GPa	s.o.f	x	y	z	Ueq or Uiso	
Cs1	0.760(15) Cs, 0.240(15) K	0	0	1/4	0.0202(2)	
Cs2	0.857(8) Cs, 0.143(8) K	2/3	1/3	0.2464(2)	0.0202(2)	
Si1	1	0.1797(4)	0.4509(4)	0.5054(5)	0.0057(3)	
Si2	1	0.1627(3)	0.2207(4)	0.5003(5)	0.0057(3)	
Si3	1	0.3942(4)	0.5092(4)	0.5076(5)	0.0057(3)	
Be1	2/3 Be, 1/3 B	0.1673(13)	0.3395(13)	0.7617(12)	0.0052(3)	
Be2	2/3 Be, 1/3 B	0.498(2)	0	3/4	0.0052(3)	
Mg1	0.975(16) Mg, 0.025(16) Fe	0	0.3324(7)	3/4	0.0086(5)	
Mg2	0.758(15) Mg, 0.242(15) Fe	0.3301(5)	0.3301(5)	3/4	0.0086(5)	
O1a	1	0.1302(8)	0.3901(8)	0.6563(10)	0.0078(5)	
O1b	1	0.1240(7)	0.3696(8)	0.3676(11)	0.0078(5)	
O1c	1	0.1889(7)	0.2706(8)	0.6595(9)	0.0078(5)	
O1d	1	0.2106(7)	0.2803(7)	0.3543(11)	0.0078(5)	
O1e	1	0.4553(7)	0.0429(8)	0.6227(11)	0.0078(5)	
O1f	1	0.4778(6)	0.0767(6)	0.3212(8)	0.0078(5)	
O2a	1	0.2895(9)	0.4944(8)	0.4687(7)	0.0078(5)	
O2b	1	0.4543(7)	0.6218(8)	0.5028(11)	0.0078(5)	
O2c	1	0.1769(7)	0.1317(8)	0.4925(10)	0.0078(5)	
	U^{11}	U^{22}	U^{33}	U^{12}	U^{13}	U^{23}
Cs1	0.0228(3)	0.0228(3)	0.0149(3)	0.01139(14)	0	0
Cs2	0.0228(3)	0.0228(3)	0.0149(3)	0.01139(14)	0	0

693
 694
 695
 696

697 **Table S4 (deposited).** Selected cation-oxygen bond distances (Å).
 698
 699

700	<i>P</i> (GPa)	(Cs,K)	(Be,B)	Si	(Mg,Fe)
701	0.0001 GPa	<i>Cs-O2</i> 3.396(2) 12×	<i>Be-O1</i> 1.5872(6) 4×	<i>Si-O1</i> 1.6063(6) 2×	<i>Mg-O1</i> 2.0909(7) 6×
702	(P6/mcc)			<i>Si-O2</i> 1.6161(9)	
703				<i>Si-O2'</i> 1.6170(11)	
704					
705	1.65(5) GPa	<i>Cs-O2</i> 3.386(4) 12×	<i>Be-O1</i> 1.583(4) 4×	<i>Si-O1</i> 1.605(3) 2×	<i>Mg-O1</i> 2.078(5) 6×
706	(P6/mcc)			<i>Si-O2</i> 1.610(7)	
707				<i>Si-O2'</i> 1.619(7)	
708					
709	6.50(5) GPa	<i>Cs1-O2c</i> 3.346(11) 6×	<i>Be1-O1a</i> 1.54(3)	<i>Si1-O1a</i> 1.613(10)	<i>Mg1-O1a</i> 2.003(11) 2×
710	(P $\bar{3}c1$)	<i>Cs1-O2c'</i> 3.433(11) 6×	<i>Be1-O1b</i> 1.45(2)	<i>Si1-O1b</i> 1.685(11)	<i>Mg1-O1d</i> 1.940(15) 2×
711		<i>Cs2-O2a</i> 3.143(12) 3×	<i>Be1-O1c</i> 1.60(2)	<i>Si1-O2a</i> 1.578(14)	<i>Mg1-O1e</i> 2.075(16) 2×
712		<i>Cs2-O2a'</i> 3.552(12) 3×	<i>Be1-O1d</i> 1.60(2)	<i>Si1-O2b</i> 1.636(17)	<i>Mg2-O1b</i> 2.054(19) 2×
713		<i>Cs2-O2b</i> 3.256(13) 3×	<i>Be2-O1e</i> 1.64(2) 2×	<i>Si2-O1c</i> 1.572(10)	<i>Mg2-O1c</i> 2.136(12) 2×
714		<i>Cs2-O2b'</i> 3.266(13) 3×	<i>Be2-O1f</i> 1.60(2) 2×	<i>Si2-O1d</i> 1.565(10)	<i>Mg2-O1f</i> 2.158(11) 2×
715				<i>Si2-O2c</i> 1.564(16)	
716				<i>Si2-O2c'</i> 1.661(17)	
717				<i>Si3-O1e</i> 1.558(15)	
718				<i>Si3-O1f</i> 1.620(10)	
719				<i>Si3-O2a</i> 1.620(16)	
720			<i>Si3-O2b</i> 1.575(12)		
721					
722					

723
 724
 725
 726
 727
 728

729 **Table S5 (deposited).** Unit-cell parameters, c/a ratio, unit-cell volumes, and unit-cell volume per
 730 formula unit (V/Z) of johnkoivulaite, in addition to the unit-cell volume of the quartz used as pressure
 731 calibrant under static hydrostatic pressures at 298 K.
 732
 733

734	V_{Qz} (Å ³)	P (GPa)	a (Å)	c (Å)	c/a' *	V (Å ³)	V/Z (Å ³)
735							
736	111.634(4)	0.457(3)	9.4654(8)	9.0323(8)	0.9542	700.83(13)	350.41(7)
737	110.037(9)	1.034(8)	9.4502(5)	9.0214(4)	0.9546	697.73(8)	348.87(4)
738	108.188(5)	1.839(4)	9.4349(6)	9.0049(4)	0.9544	694.20(9)	347.10(5)
739	107.574(4)	2.118(4)	9.4298(7)	8.9983(5)	0.9542	692.94(10)	346.47(5)
740	106.626(8)	2.570(8)	9.4207(4)	8.9879(3)	0.9541	690.81(6)	345.40(3)
741	105.578(5)	3.100(5)	9.4091(5)	8.9767(4)	0.9540	688.25(7)	344.14(3)
742	104.732(10)	3.553(11)	9.4001(5)	8.9657(3)	0.9538	686.09(7)	343.05(3)
743	103.765(9)	4.098(9)	16.2622(6)	8.9515(5)	0.9534	2050.17(18)	341.70(3)
744	102.643(6)	4.769(7)	16.2290(5)	8.9285(4)	0.9529	2036.52(15)	339.42(3)
745	101.783(4)	5.313(4)	16.2003(8)	8.9067(6)	0.9523	2024.39(24)	337.40(4)
746	100.847(8)	5.935(8)	16.1721(14)	8.8844(5)	0.9515	2012.28(22)	335.38(4)
747	99.955(11)	6.558(26)	16.1403(5)	8.8610(4)	0.9509	1999.11(16)	333.19(3)
748	99.350(9)	6.998(21)	16.1200(7)	8.8462(5)	0.9505	1990.75(19)	331.79(3)
749	n.d.* *	7.50(7)	16.0972(10)	8.8306(7)	0.9502	1981.62(30)	330.27(5)
750	n.d.* *	8.05(6)	16.0742(7)	8.8140(6)	0.9498	1972.26(21)	328.71(3)
751	n.d.* *	8.41(6)	16.0534(40)	8.7998(46)	0.9493	1963.98(1.32)	327.33(22)

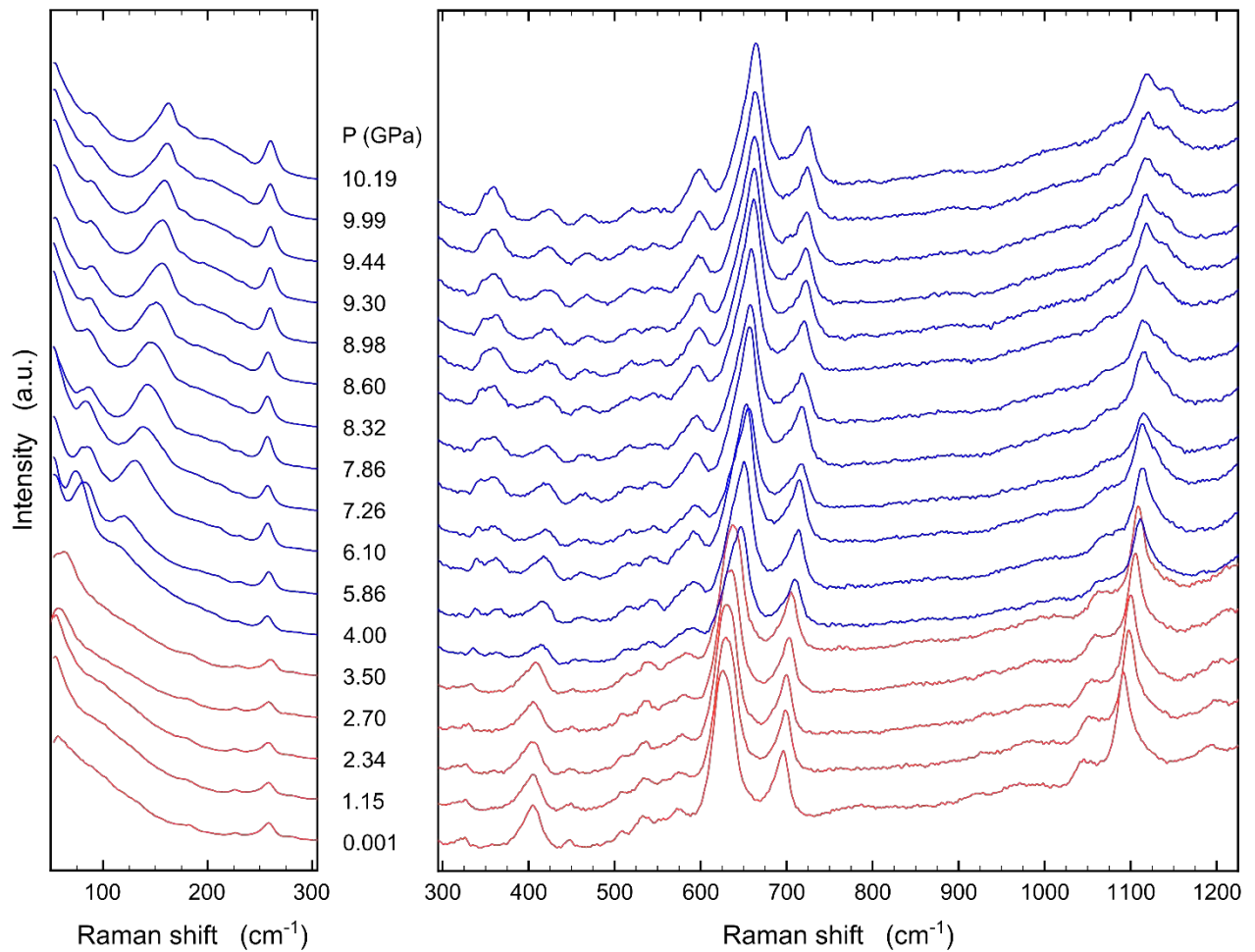
752

* $a' = a$ for $P \leq 3.553$ GPa, $a' = a/\sqrt{3}$ for $P \geq 4.098$ GPa

** n.d. = not determined; pressure was determined by the ruby-fluorescence method.

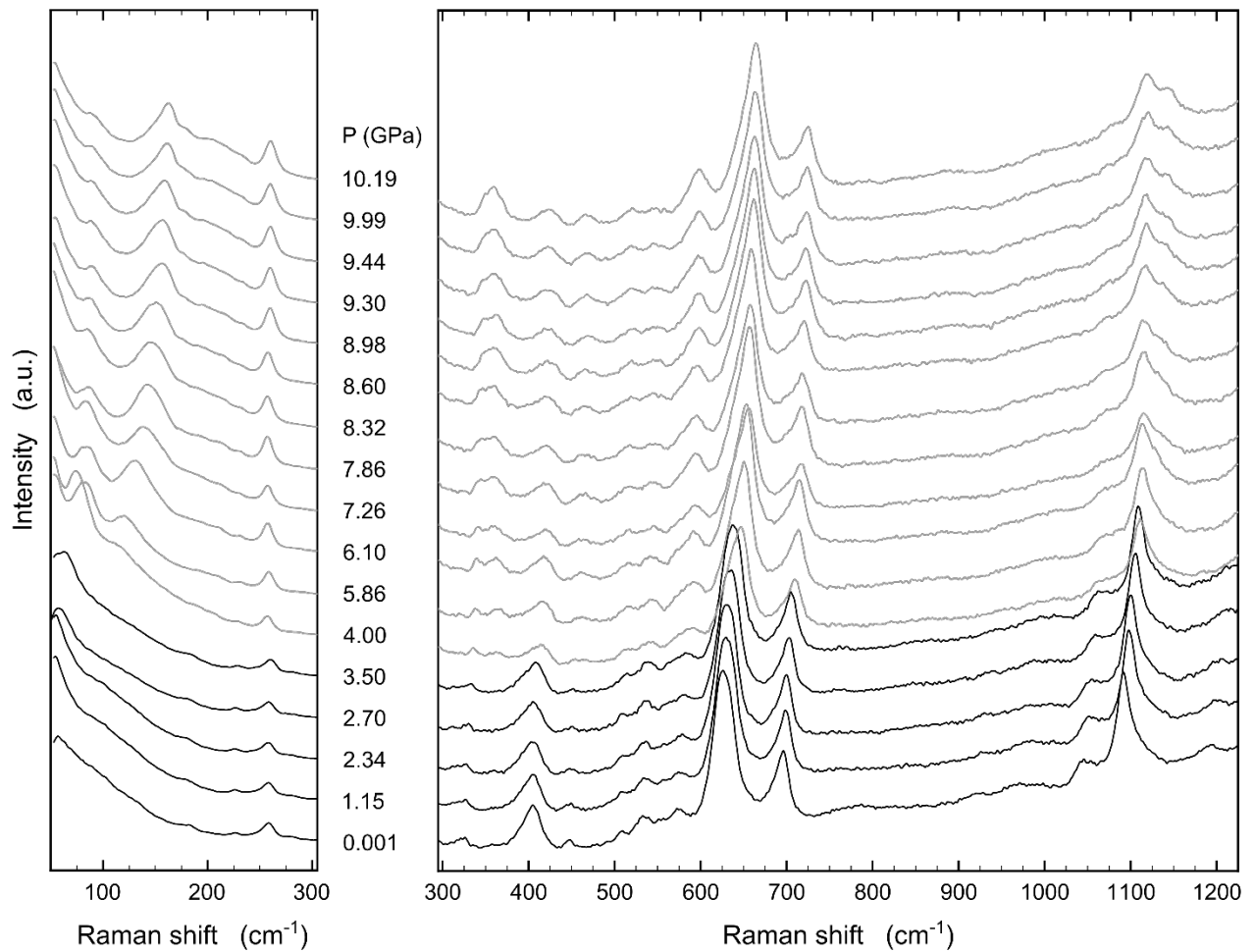
753
 754
 755
 756
 757
 758
 759
 760
 761
 762
 763
 764
 765
 766
 767
 768
 769
 770
 771
 772
 773
 774
 775
 776
 777

778 **Figure 1 (colour).** Series of 16 single-crystal Raman spectra recorded between 0.0001 and 10.19 GPa
779 of a johnkoivulaitite single crystal hydrostatically compressed in argon: entire spectral range 50-1250
780 cm^{-1} (right) and low-frequency spectral range between 50 and 300 cm^{-1} (left). Spectra of the low-*P*
781 polymorph (< 4.0 GPa) and of the high-*P* one (>4.0 GPa) are given with different colors.
782



783
784

785 **Figure 1 (B&W).** Series of 16 single-crystal Raman spectra recorded between 0.0001 and 10.19 GPa
786 of a johnkoivulaitite single crystal hydrostatically compressed in argon: entire spectral range 50-1250
787 cm^{-1} (right) and low-frequency spectral range between 50 and 300 cm^{-1} (left). Spectra of the low-*P*
788 polymorph (< 4.0 GPa) and of the high-*P* one (>4.0 GPa) are given with different colors.
789

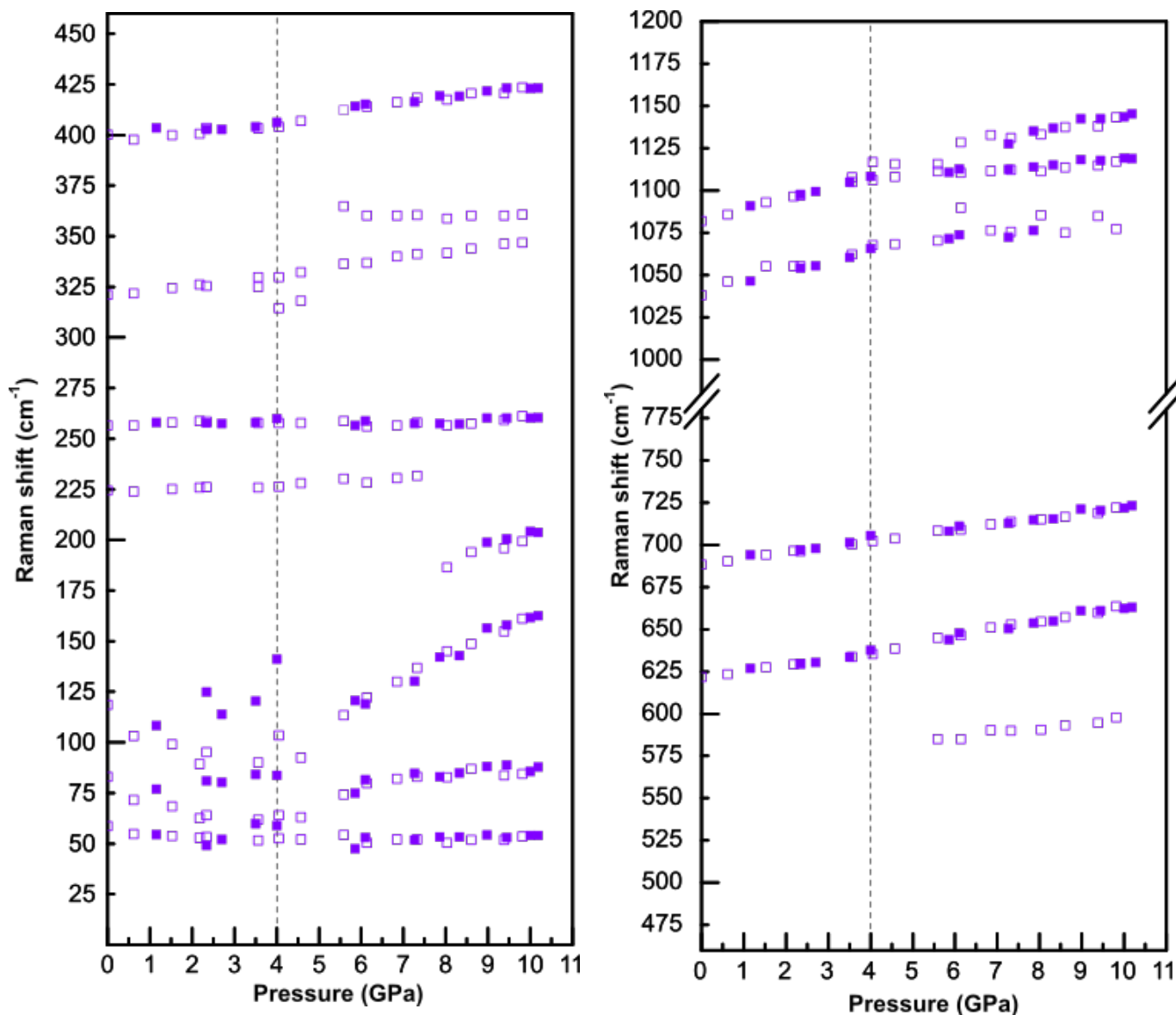


790
791
792
793
794
795
796
797
798
799
800
801
802
803

804 **Figure 2 (colour).** Pressure-induced line shifts of selected Raman modes. Values for the band
805 position were extracted from the peak fits applied to the spectra. Errors for the band positions are
806 within the size of the symbols, if not marked by error bars. The uncertainties for the pressure values
807 are within ± 0.06 GPa. The vertical line represents the assumed critical pressure for the transformation
808 at ~ 4.0 GPa. Solid symbols represent data extracted from the compression series, empty symbols
809 those obtained on decompression.

810

811



812

813

814

815

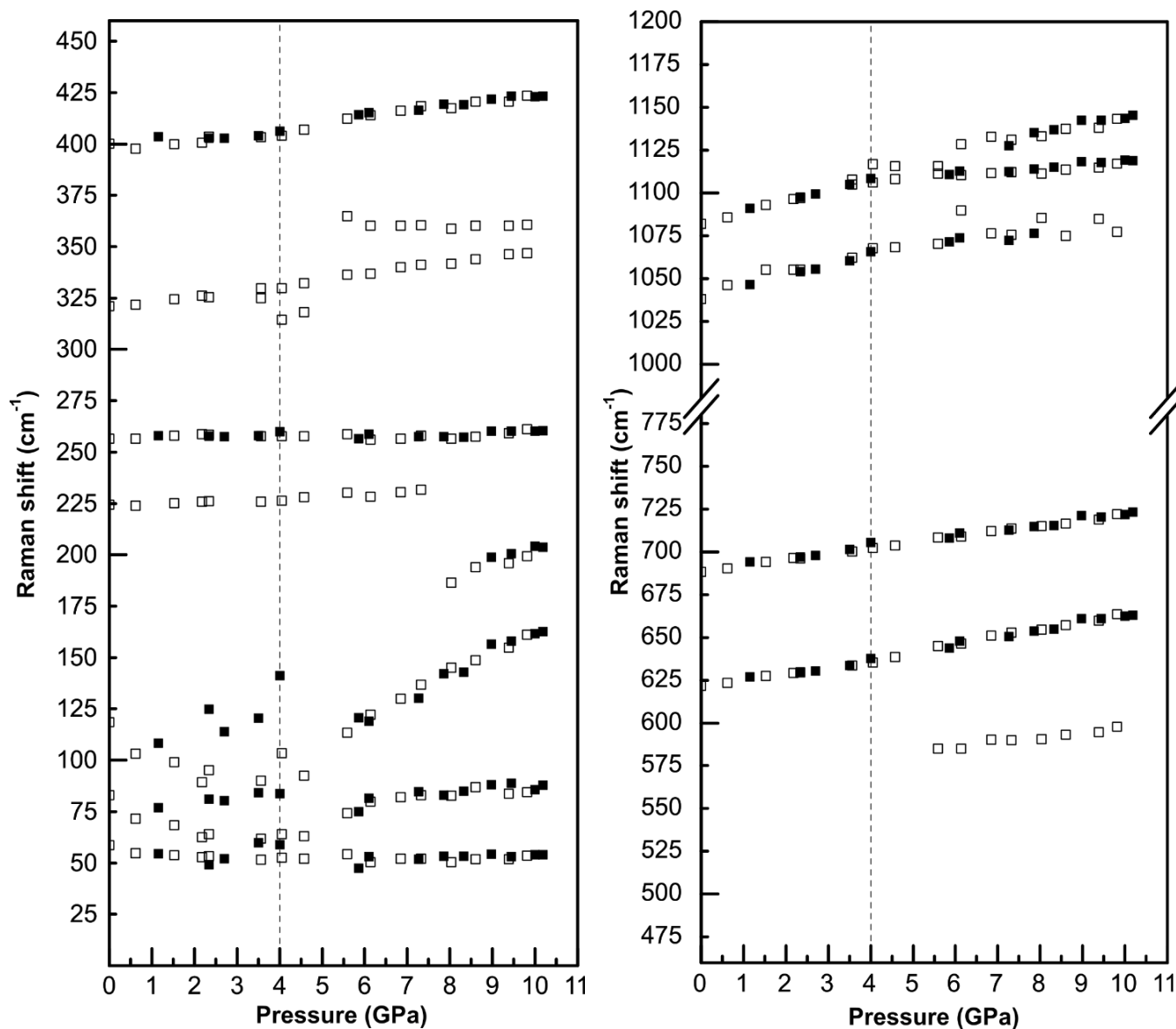
816

817

818 **Figure 2 (B&W).** Pressure-induced line shifts of selected Raman modes. Values for the band position
819 were extracted from the peak fits applied to the spectra. Errors for the band positions are within the
820 size of the symbols, if not marked by error bars. The uncertainties for the pressure values are within
821 ± 0.06 GPa. The vertical line represents the assumed critical pressure for the transformation at ~ 4.0
822 GPa. Solid symbols represent data extracted from the compression series, empty symbols those
823 obtained on decompression.

824

825



826

827

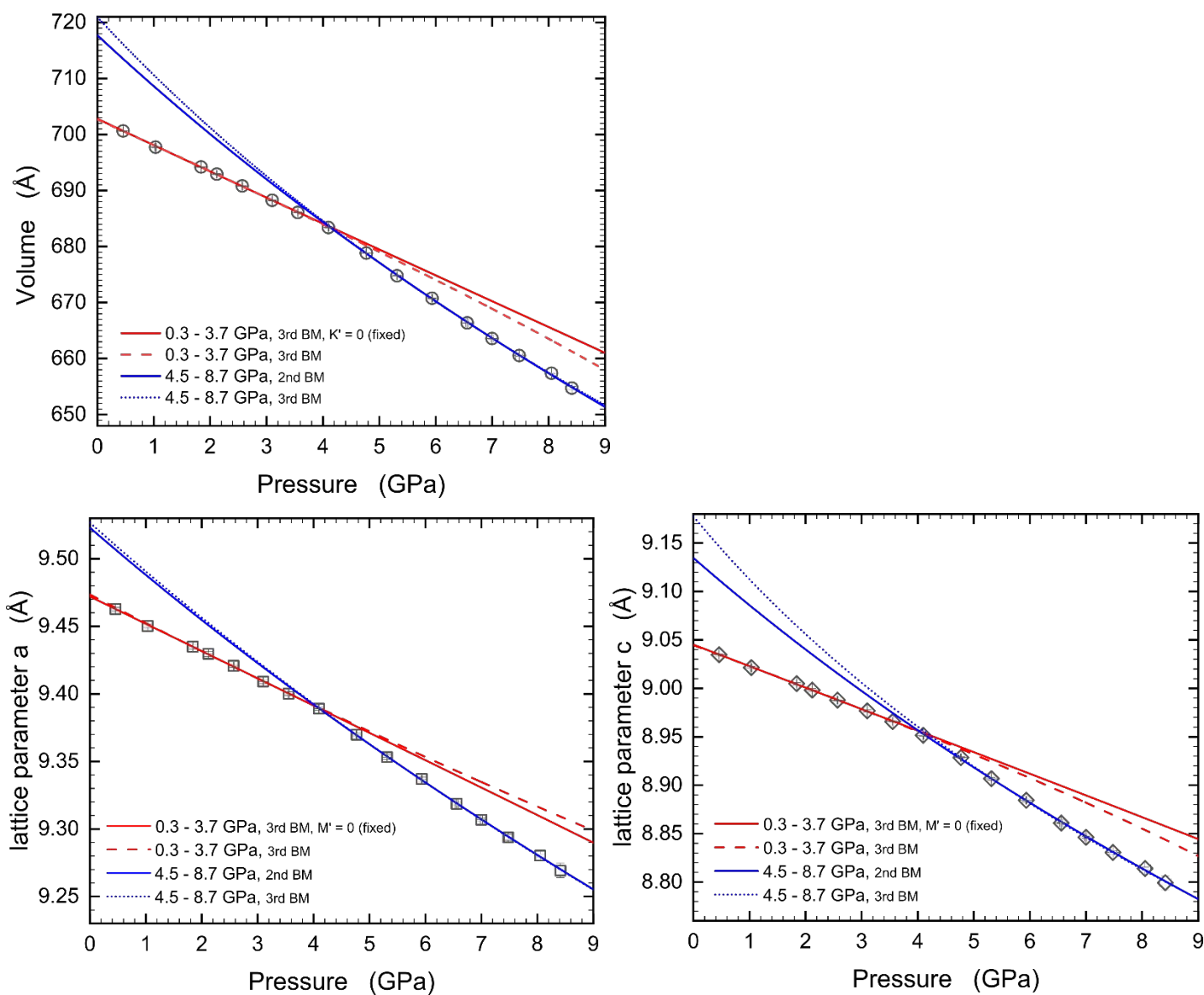
828

829

830

831

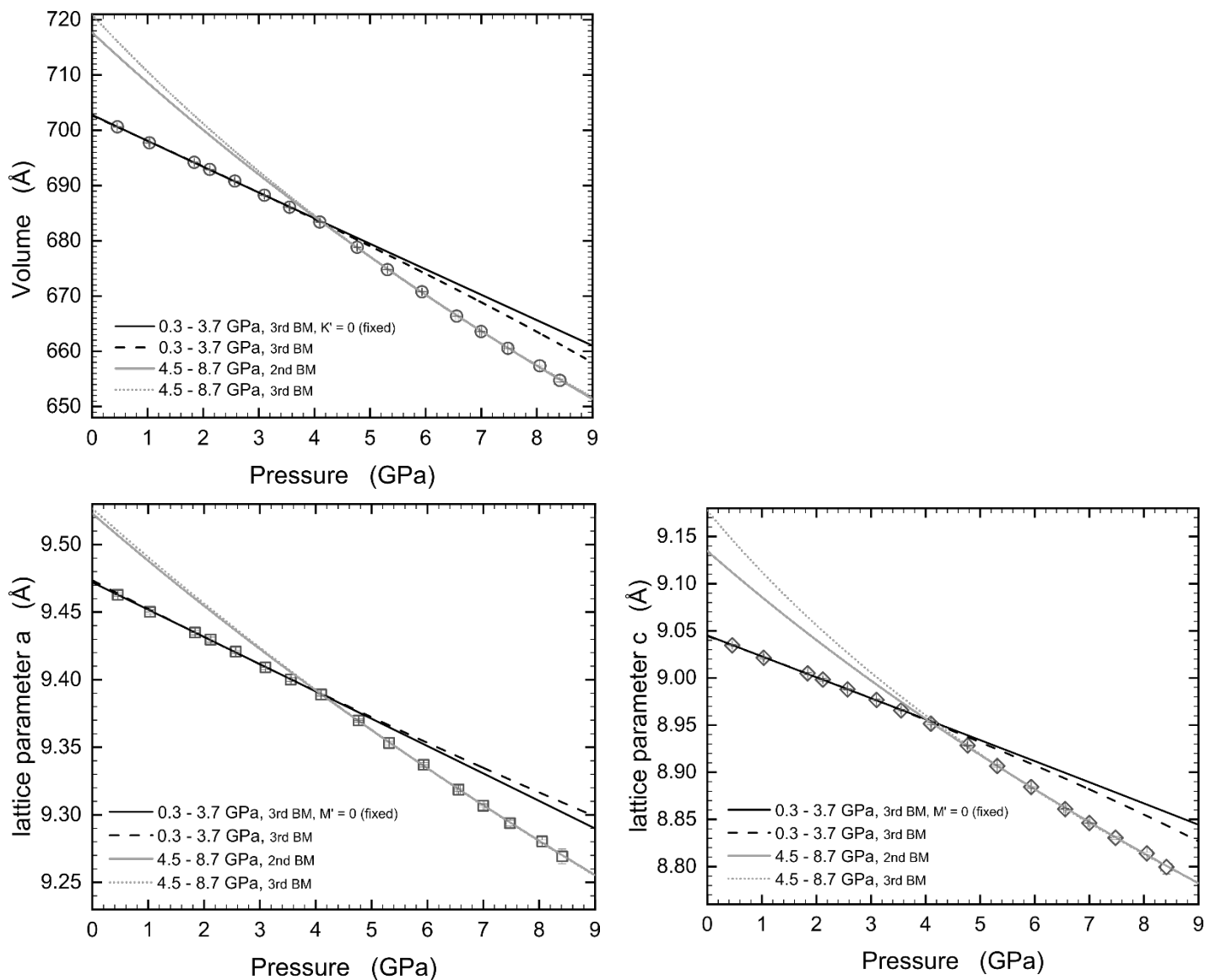
832 **Figure 3 (colour).** Pressure-dependent evolution of the unit-cell parameters a , c and the unit-cell
833 volume V , along with Birch-Murnaghan EoS fits to the experimental data. The refined BM-EoS
834 parameters are those given in Table 1.
835



836
837
838
839
840
841
842
843
844

845 **Figure 3 (B&W).** Pressure-dependent evolution of the unit-cell parameters a , c and the unit-cell
846 volume V , along with Birch-Murnaghan EoS fits to the experimental data. The refined BM-EoS
847 parameters are those given in Table 1.

848



849

850

851

852

853

854

855

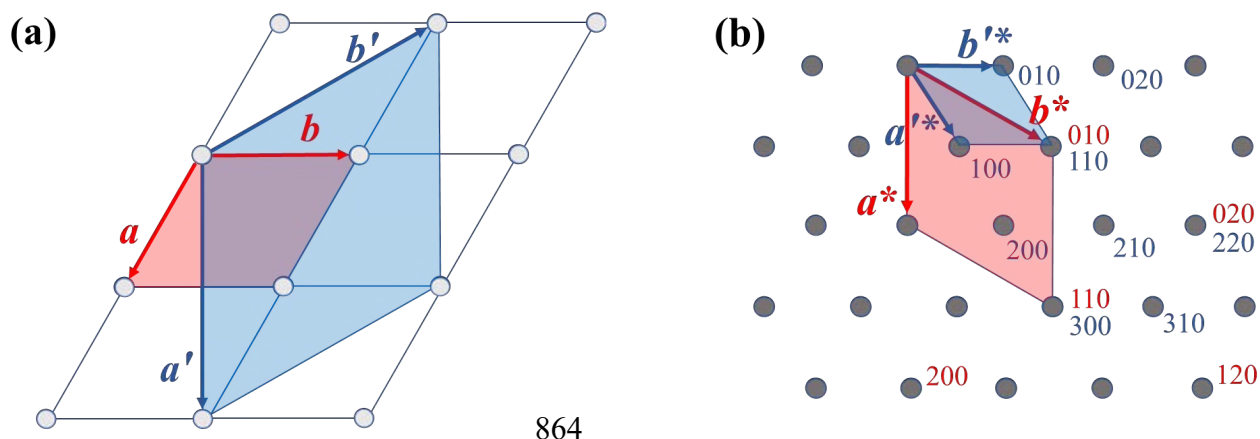
856

857

858

859 **Figure 4 (colour).** Metrical relationship between: (a) the unit cells of the the $P6/mcc$ structure (beryl-
 860 type subcell) and the $P\bar{3}c1$ superstructure (with $a' = a \cdot \sqrt{3}$, $c' = c$) in a view down the c -axis, and (b)
 861 between the two reciprocal lattices in the reciprocal space as depicted in the $hk0$ layer in a view down
 862 the c^* direction.

863



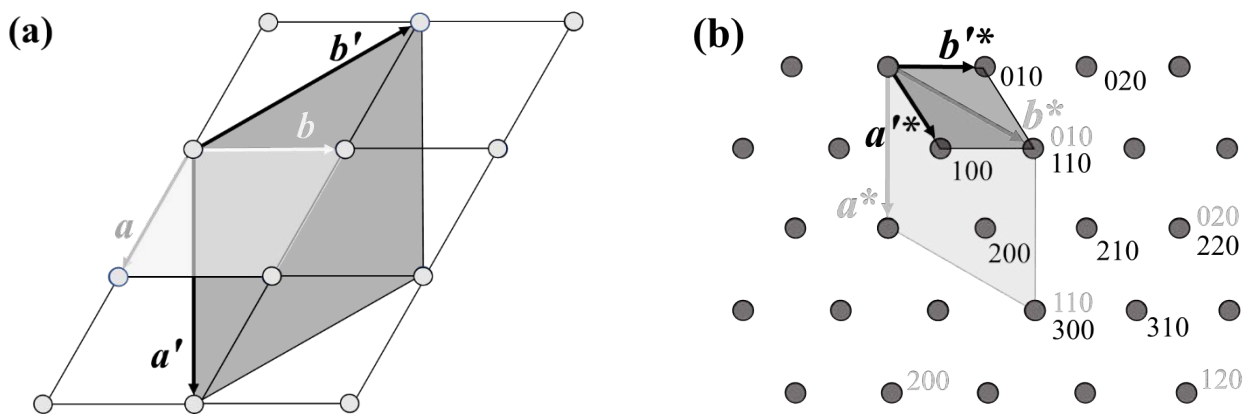
864

865

866 **Figure 4 (B&W).** Metrical relationship between: (a) the unit cells of the the $P6/mcc$ structure (beryl-
 867 type subcell) and the $P\bar{3}c1$ superstructure (with $a' = a \cdot \sqrt{3}$, $c' = c$) in a view down the c -axis, and (b)
 868 between the two reciprocal lattices in the reciprocal space as depicted in the $hk0$ layer in a view down
 869 the c^* direction.

870

871



872

873

874

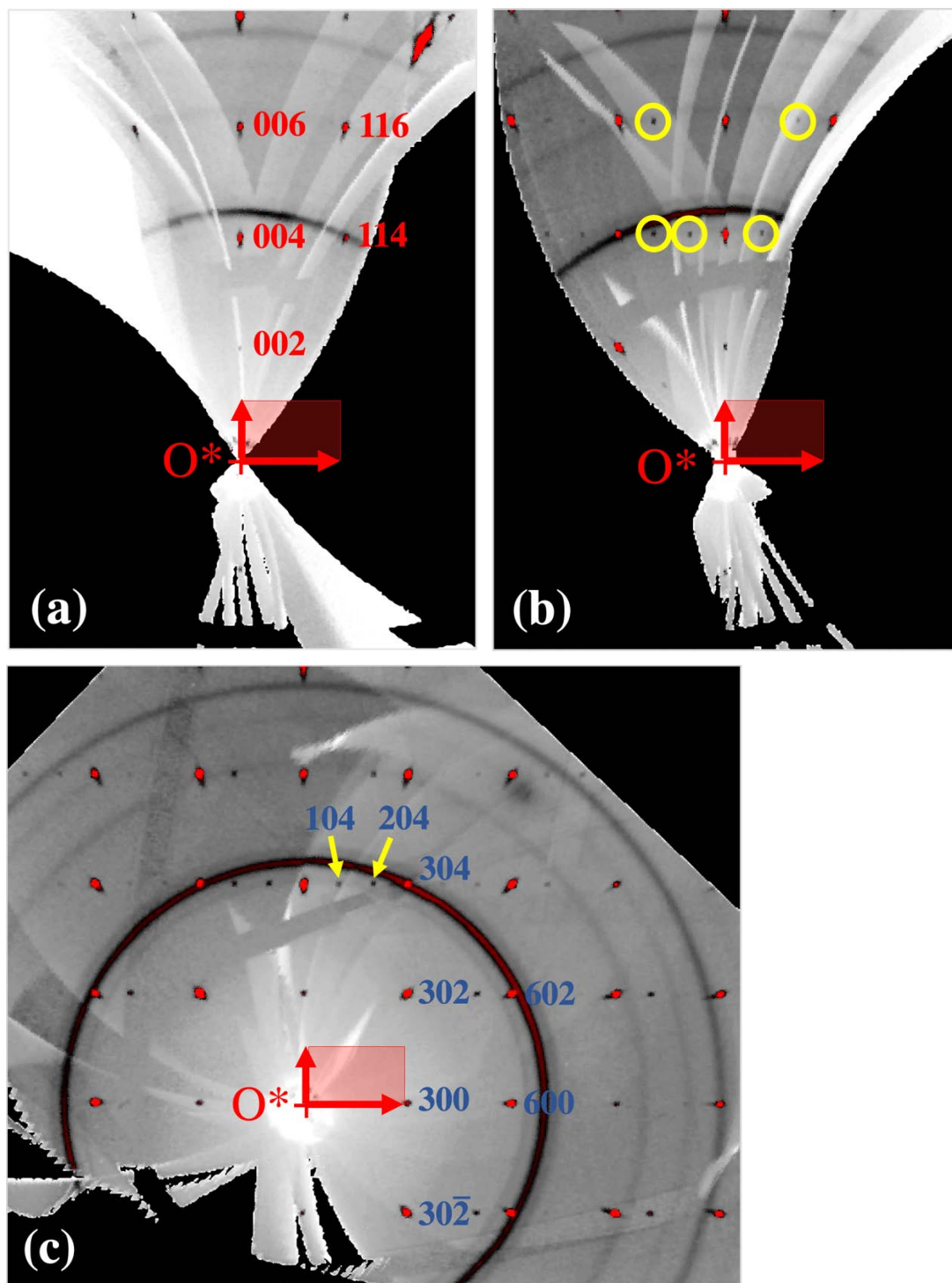
875

876

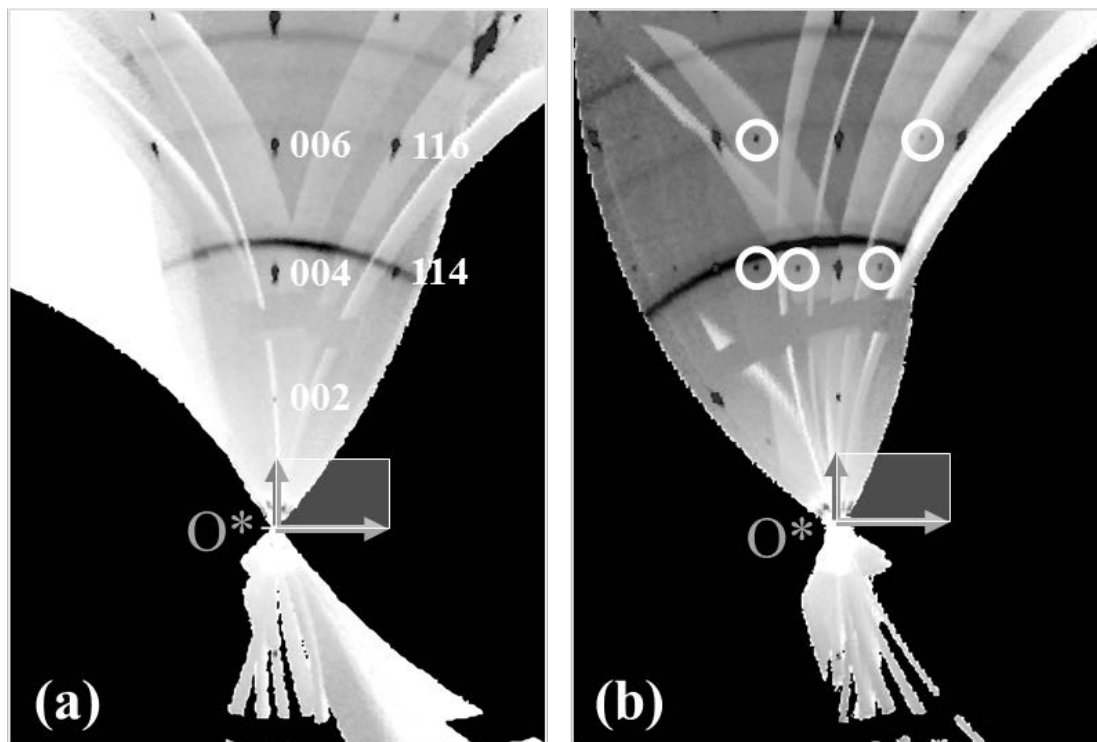
877

878

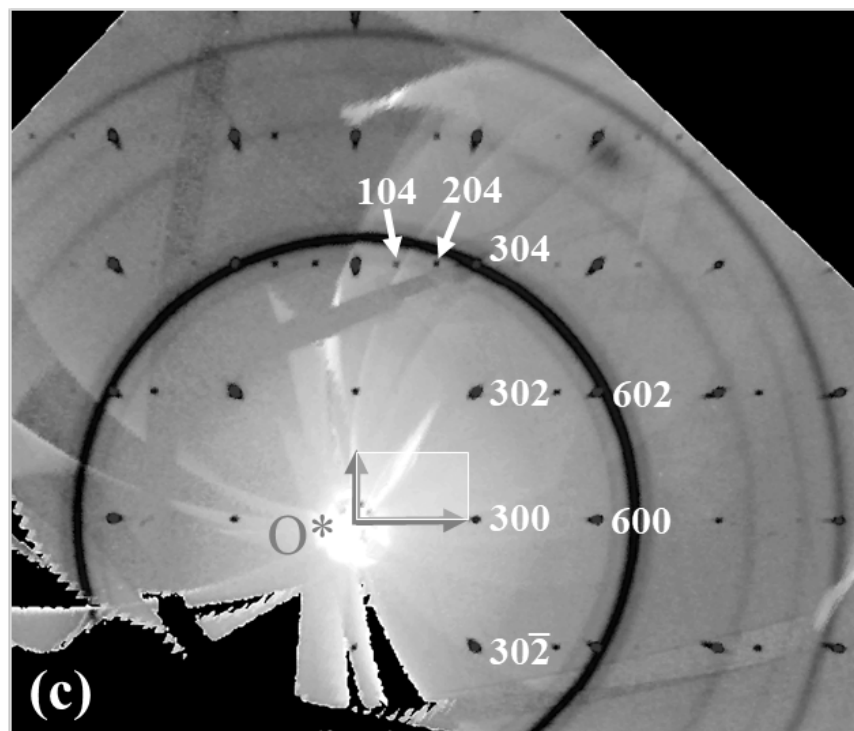
879 **Figure 5 (colour).** Reconstructed reciprocal lattice planes of the (a) *hhl* layer at $P = 1.65(6)$ GPa, (b)
880 *okl* layer at $P = 6.50(5)$ GPa, and (c) the *h0l* also at 6.50(5) GPa. The plane direction represents
881 equivalent orientations in the reciprocal space, corresponding to the c^* (vertical arrow) and d_{110}^*
882 (horizontal arrow) directions of the hexagonal beryl-type subcell. Indices in (a) are based on this
883 subcell, indices in (c) correspond to the $P\bar{3}c1$ superstructure ($a' = a\sqrt{3}$, $c' = c$). Circles mark the
884 superstructure reflections, which appear at pressures above $P_c \approx 4.0$ GPa. Apart from the sample
885 Bragg peaks, the images show Debye rings centered in O^* , which originate from scattering of the
886 metal gasket of the diamond anvil cell.
887



891 **Figure 5 (B&W).** Reconstructed reciprocal lattice planes of the (a) *hhl* layer at $P = 1.65(6)$ GPa, (b)
892 *okl* layer at $P = 6.50(5)$ GPa, and (c) the *h0l* also at 6.50(5) GPa. The plane direction represents
893 equivalent orientations in the reciprocal space, corresponding to the c^* (vertical arrow) and d_{110}^*
894 (horizontal arrow) directions of the hexagonal beryl-type subcell. Indices in (a) are based on this
895 subcell, indices in (c) correspond to the $P\bar{3}c1$ superstructure ($a' = a\sqrt{3}$, $c' = c$). Circles mark the
896 superstructure reflections, which appear at pressures above $P_c \approx 4.0$ GPa. Apart from the sample
897 Bragg peaks, the images show Debye rings centered in O^* , which originate from scattering of the
898 metal gasket of the diamond anvil cell.
899



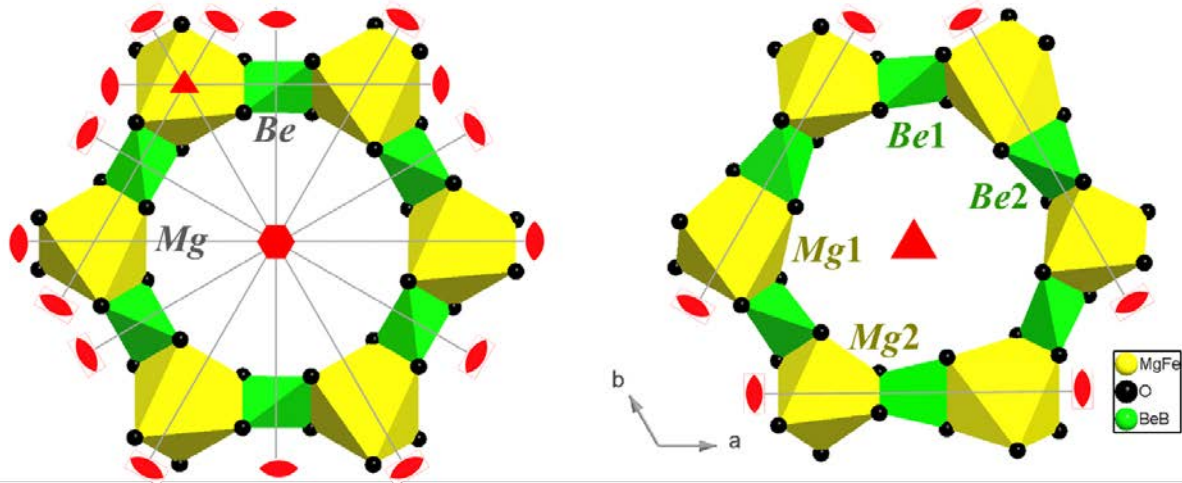
912



924

925 **Figure 6 (colour).** Di-trigonal deformation of the 12-membered ring (made by Mg,Fe-octahedra and
926 B,Be-tetrahedra) in response to the *P*-induced phase transition in johnkoivulaite, viewed down [0001]
927 (left side: at 0.0001 GPa; right side: at 6.50 GPa). Symmetry symbols indicate the presence of six-,
928 three- and two-fold axis. The phase transition leads to a reduction of point symmetries from 32 (*Mg*)
929 to .2. (*Mg1* and *Mg2*), 222 (*Be*) to 1 (*Be1*) and .2. (*Be2*).

930



931

932

933

934

935 **Figure 6 (B&W).** Di-trigonal deformation of the 12-membered ring (made by Mg,Fe-octahedra and
936 B,Be-tetrahedra) in response to the *P*-induced phase transition in johnkoivulaite, viewed down [0001]
937 (left side: at 0.0001 GPa; right side: at 6.50 GPa). Symmetry symbols indicate the presence of six-,
938 three- and two-fold axis. The phase transition leads to a reduction of point symmetries from 32 (*Mg*)
939 to .2. (*Mg1* and *Mg2*), 222 (*Be*) to 1 (*Be1*) and .2. (*Be2*).

